



저작자표시-비영리-변경금지 2.0 대한민국

이용자는 아래의 조건을 따르는 경우에 한하여 자유롭게

- 이 저작물을 복제, 배포, 전송, 전시, 공연 및 방송할 수 있습니다.

다음과 같은 조건을 따라야 합니다:



저작자표시. 귀하는 원저작자를 표시하여야 합니다.



비영리. 귀하는 이 저작물을 영리 목적으로 이용할 수 없습니다.



변경금지. 귀하는 이 저작물을 개작, 변형 또는 가공할 수 없습니다.

- 귀하는, 이 저작물의 재이용이나 배포의 경우, 이 저작물에 적용된 이용허락조건을 명확하게 나타내어야 합니다.
- 저작권자로부터 별도의 허가를 받으면 이러한 조건들은 적용되지 않습니다.

저작권법에 따른 이용자의 권리는 위의 내용에 의하여 영향을 받지 않습니다.

이것은 [이용허락규약\(Legal Code\)](#)을 이해하기 쉽게 요약한 것입니다.

[Disclaimer](#)

공학석사 학위논문

A Basic Study on the Injection-induced Seismicity During Shut-in Stage

유체 주입 중단 후에 발생하는 유발지진에 관한
기초 연구

2018 년 8 월

서울대학교 대학원

에너지시스템공학부

임 주 휘

A Basic Study on the Injection-induced Seismicity During Shut-in Stage

유체 주입 중단 후에 발생하는 유발지진에 관한
기초 연구

지도 교수 민 기 복

이 논문을 공학석사 학위논문으로 제출함
2018 년 8 월

서울대학교 대학원
에너지시스템공학부
임 주 휘

임주휘의 공학석사 학위논문을 인준함
2018 년 8 월

위 원 장 전 석 원 (인)

부위원장 민 기 복 (인)

위 원 송 재 준 (인)

Abstract

A Basic Study on the Injection-induced Seismicity During Shut-in Stage

Ju Hyi Yim

Department of Energy Systems Engineering
Rock Mechanics & Rock Engineering Laboratory
The Graduate School
Seoul National University

Fluid injection is a crucial component of various industries related to deep underground engineering such as waste water disposal, CO₂ geosequestration, and geothermal energy. However, injection can pose seismic hazard. Shutting-in the well has been an intuitive way to suppress the seismicity. However, Large Magnitude Earthquake (LME) often occurred after shutting-in the injection in many enhanced geothermal system (EGS) sites. In Basel, particularly, EGS project was ceased due to M_L3.4 LME, which was the largest earthquake during the project and occurred five hours after shut-in. To mitigate this problem, understanding the physical mechanism of induced seismicity is necessary. In this study, the impermeable fractured rock was assumed and the pressure gradient effect was shown by the semi-analytic approach. As a numerical approach, two dimensional discrete element modeling is conducted for the hydro-mechanically coupled analysis. By generating and

simulating the multiple fractures, the fault interaction was suggested as one of the mechanisms that induce earthquake during shut-in stage.

Keyword : Large Magnitude Earthquake, Enhanced Geothermal System, Hydraulic Stimulation, Induced Seismicity

Student Number : 2016-23992

Table of Contents

Chapter 1. Introduction.....	1
1.1. Background.....	1
1.2. Objective.....	3
Chapter 2. Literature Review.....	4
2.1. Induced Seismicity in EGS.....	4
2.2. Basel, Switzerland.....	5
2.2.1. <i>The brief information about hydraulic stimulation.....</i>	<i>5</i>
2.2.2. <i>Characteristics of LMEs.....</i>	<i>6</i>
2.2.3. <i>Fault system.....</i>	<i>8</i>
2.3. Soultz–sous–forêts, France.....	9
2.3.1 <i>The brief information of hydraulic stimulation.....</i>	<i>9</i>
2.3.2 <i>Characteristics of LMEs.....</i>	<i>9</i>
2.3.3 <i>Fault system.....</i>	<i>12</i>
2.4. Cooper Basin, Australia.....	13
2.5. Characteristics of LMEs during shut–in stage.....	14
2.6. Previous studies.....	16
2.6.1. <i>Pore pressure gradient effect.....</i>	<i>16</i>
2.6.2. <i>Unstable rupture propagation.....</i>	<i>17</i>
2.6.3. <i>Numerical studies.....</i>	<i>19</i>
Chapter 3. Semi–analytical approach for magnitude estimation during shut–in stage.....	20
3.1. Model description.....	20
3.2. Result.....	26
Chapter 4. Numerical simulation for hydro–mechanical analysis of induced seismicity.....	33
4.1. Description of numerical code, UDEC.....	33
4.2. Stress redistribution on the single fault.....	34
4.3. Stress redistribution on the multi fracture.....	37
4.4. Application to Basel case.....	41
Chapter 5. Conclusion.....	49
Bibliography	50
초 록	55

Lists of Tables

Table 1 Input parameters for semi-analytical solution	25
Table 2 Input parameters for UDEC simulation.....	45

Lists of Figures

Figure 1.1: Mohr circle representations of the state of stress at the occurring moment of seismicity.....	2
Figure 1.2: Maximum magnitude of earthquake along the injected volume (McGarr, 2014).....	2
Figure 2.1: (a) Well-head pressure and injection rate histories in Basel. (b) Local magnitudes of the induced events. (c) Events per hour with moment magnitudes greater than 0.8 (Deichmann et al., 2014).....	5
Figure 2.2: Injection history and snapshots of spatial pore pressure distribution in Basel (Mukuhira et al., 2017).....	7
Figure 2.3: (Left) Fracture system in Basel (E–W section view). (Right) Plane view of Faults located below the casing shoe and in the south–eastern part in the red box of the left figure. The red dot in the right figure and the red line in the left figure depict the injection hole. (Kraft et al., 2014; Deichmann et al., 2014; Mukuhira et al., 2017)	8
Figure 2.4: (a) (Top) The seismic history of events larger than or equal to 1.4 for GPK2 stimulation in 2000. (Bottom) The injection history of flow rate and wellhead pressure. (b) (Top) The seismic history of events larger than or equal to 1.4 for GPK3 stimulation in 2003. (Bottom) The injection history of flow rate and wellhead pressure (Charl��ty et al, 2007).....	10
Figure 2.5: (c) (Top) The seismic history of events larger than or equal to 1.4 for GPK4 stimulation in 2004. (Bottom) The injection history of flow rate and wellhead pressure. (d) (Top) The seismic history of events larger than or equal to 1.4 for GPK4 stimulation in 2004. (Bottom) The injection history of flow rate and wellhead pressure (Charl��ty et al, 2007).....	11
Figure 2.6: 3D views of defined faults in Soultz–sous–for��ts (Sausse et al., 2010).....	12
Figure 2.7: Hypocenter locations of seismic events from the 2003 stimulation of Habanero 1. The origin point is the location of	

Habanero 1 (McMahon et al., 2013).	13
Figure 2.8: The graph of the largest magnitude after shut-in. The start of arrow indicates the largest magnitude during injection, and the end of arrow indicates the largest magnitude during shut-in stage. The number in the bracket indicates the total injected volume(m^3) until each event. 1) : Mukuhira et al.(2017), 2) : Charl�ty et al.(2007), 3) : Asanuma et al.(2005), 4) : Baisch et al.(2015).....	14
Figure 2.9: Schematic diagram of the mechanism of pore pressure gradient effect(Mukuhira et al, 2017).	16
Figure 2.10: The stable and unstable rupture diagram along the pore pressure change(Galis et al., 2017).....	18
Figure 2.11: The general rupture profile with the shear dilation effect (Norbeck et al., 2018).....	18
Figure 3.1: The schematic diagram of the semi-analytical model.	21
Figure 3.2: The radius histories of stimulated zone for the same injected fluid volume.....	23
Figure 3.3: The pressure profiles of the semi-analytical solution (Black) at the moment of shut-in, (Red) during shut-in stage, and (Blue) under the condition of no shut-in. (Dashed line) the critical pore pressure interval for determining the possible slip area.	26
Figure 3.4: (Top Left) The histories of the pore pressure over the hydrostatic pressure at the injection point. (Bottom Left) The possible magnitude jump history with the black vertical line indicating the shut-in moment. (Bottom Right) The possible magnitude jump profile. The possible magnitude jump is calculated based on the maximum possible slip area before shut-in at each case. Different apertures in the unstimulated area were applied in each case.....	29
Figure 3.5: (Top Left) The histories of the pore pressure over the hydrostatic pressure at the injection well. (Bottom Left) The possible magnitude jump history with the black vertical line indicating the shut-in moment. (Bottom Right) The possible magnitude jump profile. The possible magnitude jump is	

calculated based on the maximum possible slip area before shut-in at each case. Different apertures in the stimulated area were applied in each case.....	30
Figure 3.6: (Top Left) The histories of the pore pressure over the hydrostatic pressure at the injection well. (Bottom Left) The possible magnitude jump history with the black vertical line indicating the shut-in moment. (Bottom Right) The possible magnitude jump profile. The possible magnitude jump is calculated based on the maximum possible slip area before shut-in at 0.0268m ³ /s case because the fault properties are same. Different flow rate and injection period to conserve the total injected volume are applied in each case.....	31
Figure 4.1: The schematic diagram for single fracture simulation.	33
Figure 4.2: The UDEC simulation of shear slip. (Top) The shear displacement profiles around the slipping moment. (Middle) The shear stress and normal stress profiles around the slipping moment. (Bottom) The critical pore pressure and pore pressure profiles around the slipping moment. The time difference between the adjacent thin line is 1.7s and every 5th line is thickened. The passage of time is indicated by the brightness of the color.....	34
Figure 4.3: Model for shear slip simulation. Uniformly distributed pore pressure is given in the fault centered in the model, and induced the slip. (Stress Drop, $\Delta \tau$)=3.7395MPa.....	39
Figure 4.4: Δ CFS profiles normalized by stress drop along each hypothetical fault. A-1,2,3 are profiles from the fault group starting from point A. B-1,2,3 are profiles from the fault group starting from point B. D is the distance from the intersection point(A or B). Each axis is normalized by the stress drop and the half length of fault respectively.	40
Figure 4.5: Stress change on the direction of the hypothetical fault(Case A-1,B-1).....	41
Figure 4.6: Stress change on the direction of the hypothetical fault(Case A-2, B-2).	42
Figure 4.7: Stress change on the direction of the hypothetical	

fault (Case A-3, B-3).	43
Figure 4.8: UDEC model. Simplified fault system in Basel (Figure 2.3).....	44
Figure 4.9: (Left) The critical pore pressure profiles and (Right) the normal and shear stress change profiles on the connected faults in both cases	44
Figure 4.10: Seismic histories of case 1 and 2.....	46
Figure 4.11: Pressure profiles along the connected fault in Case 1.	46
Figure 4.12: Pressure profiles along the connected fault in Case 2.	47

Chapter 1. Introduction

1.1. Background

Fluid injection is common in energy-related subsurface industries such as Enhanced Geothermal System(EGS), Enhanced Oil Recovery(EOR), and CO₂ geosequestration(Ellsworth, 2013). Each fluid-injecting industry has its own purpose of fluid injection, and the characteristics of fluid injection vary with its purpose. In wastewater disposal and CO₂ geosequestration, fluid was injected into deep reservoir in order to store massive volume of fluid, so the target formation is permeable and large flow rate with relatively small pressure can be achieved. In addition, the upper limit of pressure for injection is low because the geological seal integrity should be guaranteed(Bissell et al., 2011; Tangen et al., 2013; Lutz et al., 2013; Goebel et al.,2017). By contrast, hydraulic stimulation in EGS and shale gas development injects fluid with intent to enhance the permeability of impervious reservoir. Therefore, the upper limit of pressure is higher than the fluid-storing cases and fluid injection is applied during relatively short period. Especially, in EGS case, shearing the pre-existing fault is the purpose of the hydraulic stimulation, so the intended upper limit of pressure is the critical pore pressure of main fault instead of minimum principle stress which is regarded as the target of the hydraulic fracturing(Tester, 2007).

Induced seismicity is traditional issue accompanying the fluid injection(Davis and Frohlich, 1993). As Figure 1.1 shows, the injection-induced seismicity is inevitable phenomenon that can occur because the fluid pressure decreases the effective normal stress. In addition, the magnitude of induced seismicity is significant. According to Figure 1.2, the possible maximum magnitude of seismicity is empirically proportional to the injected volume of water. Thus, wastewater disposal with large fluid injection induced bigger earthquake than EGS did.

Despite a wide application of fluid injection, its mechanism to induce earthquake is not clearly explained. In particular, enigmatic phenomenon of induced earthquake during shut-in requires substantial investigation.

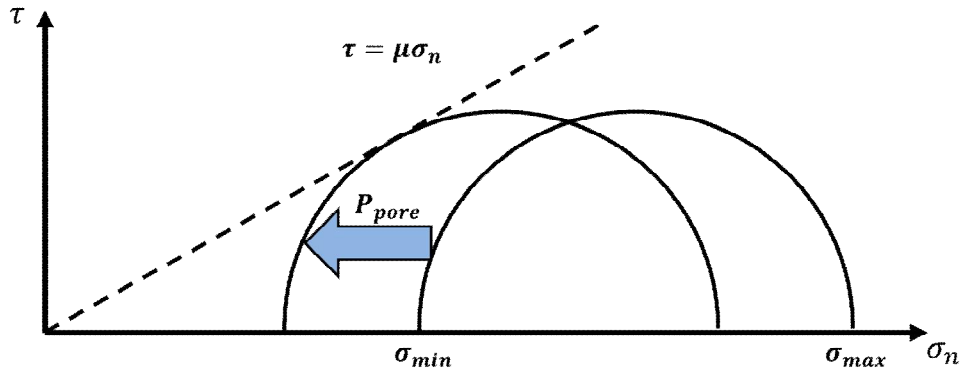


Figure 1.1: Mohr circle representations of the state of stress at the occurring moment of seismicity.

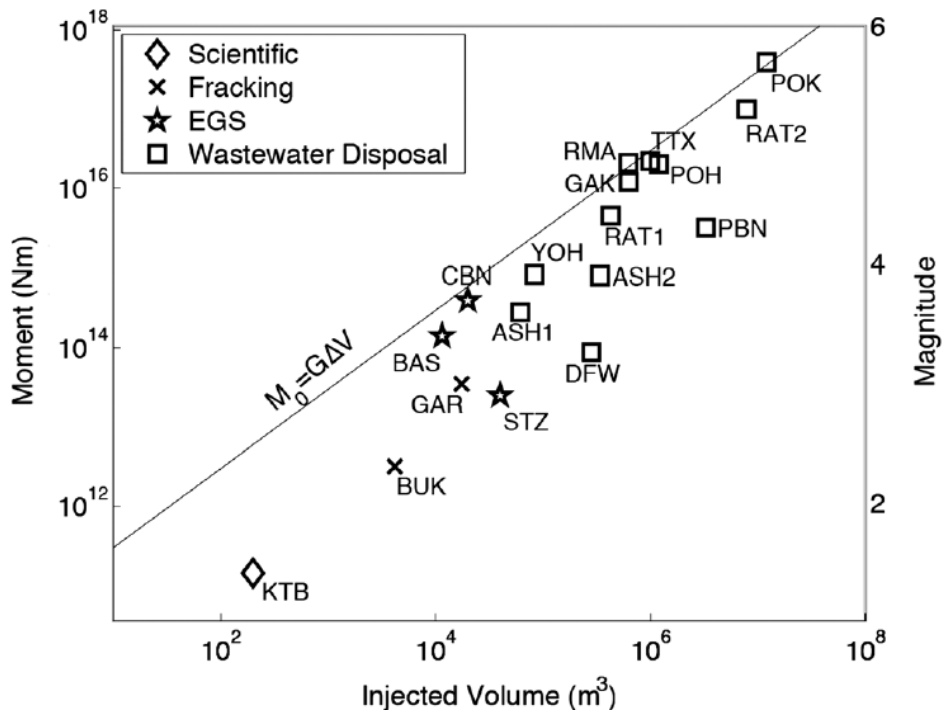


Figure 1.2: Maximum magnitude of earthquake along the injected volume (McGarr, 2014).

1.2. Objective

This paper investigates various characteristics of LMEs in several fields and the mechanism of the induced seismicity during the post injection period with the following focus;

1. Analyzing LME cases and characteristics
2. Suggesting the mechanism of LME during post injection period
3. Simulating the model corresponding to the actual fields by hydro-mechanical coupling analysis

To analyze LME cases during shut-in stage, the hydraulic stimulations and seismic data in Basel, Soultz-sous-forêts and Cooper Basin were studied. The analytic approach was applied to show the mechanism of increased magnitude after shut-in by the diffusion equation. To consider the whole mechanism comprehensively, the stress redistribution and the multi-fracture model were included in the numerical simulation. The numerical approach by 2D DEM code was conducted to investigate how the suggested mechanism affects the occurrence of LMEs during shut-in stage.

Chapter 2. Literature Review

2.1. Induced Seismicity in EGS

Due to injected fluid into the rock mass, the pore pressure increases and effective normal stress decreases eventually being able to fulfill Coulomb failure criteria, so the seismicity by the shear slip is an inevitable phenomenon (National Research Council, 2013; Walsh and Zoback, 2015). Especially, public acceptance of residents is important consideration in an EGS project because of the induced seismicity (Majer et al., 2012). In Basel, $M_L 3.4$ earthquake caused minor damages on some buildings and resulted in the suspension of Basel EGS project (Kraft et al., 2009). Thus, relieving the induced seismicity becomes more important in fluid-injecting technology, and shutting-in the well is one of the most intuitive ways to deal with LMEs (Majer et al., 2012; Kim et al., 2018). However, the largest magnitude earthquake sometimes took place in fluid-injecting sites during shut-in stage. For example, shut-in decreased the seismic rate, but the largest magnitude earthquake in Basel occurred at around 5 hours after shutting-in the well (Figure 1.1). Apart from Basel, these enigmatic phenomena were also observed in various fields such as Soultz-sous-forêts, and Cooper Basin (Asanuma et al., 2005; Baisch et al., 2006; Charléty et al., 2007). To deal with the induced seismicity appropriately, the detailed mechanism of induced seismicity needs to be clarified.

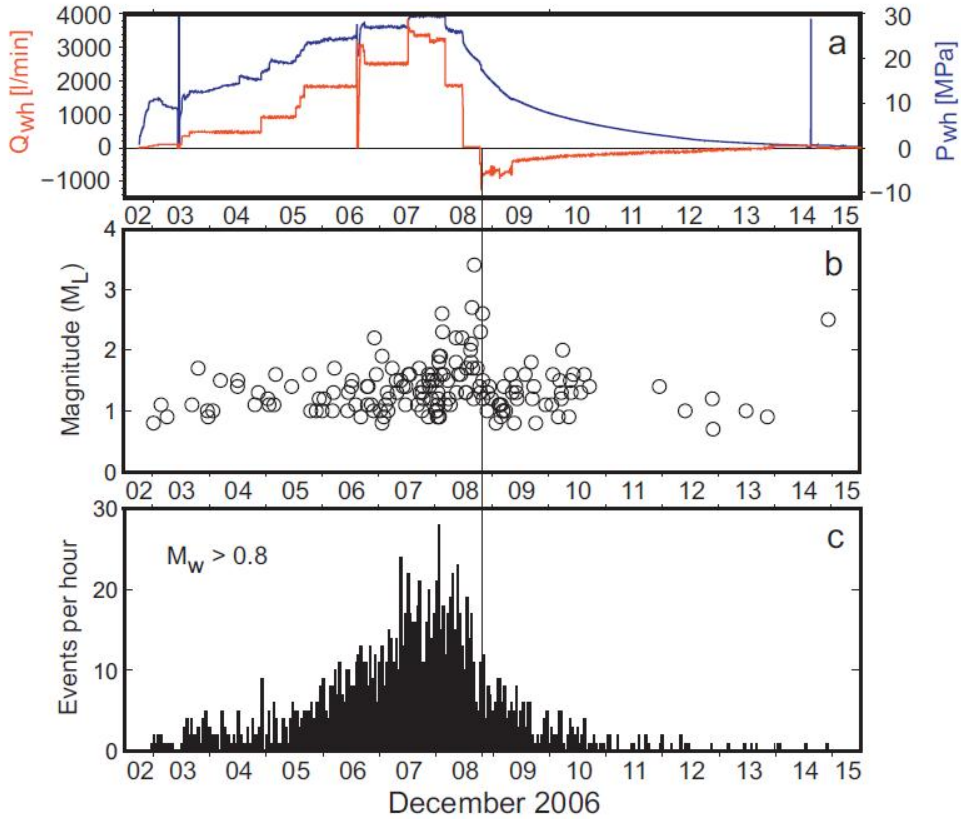


Figure 2.1: (a) Well-head pressure and injection rate histories in Basel. (b) Local magnitudes of the induced events. (c) Events per hour with moment magnitudes greater than 0.8 (Deichmann et al., 2014).

2.2. Basel, Switzerland

2.2.1. The brief information about hydraulic stimulation

In Basel, the Deep Heat Mining project which is the EGS project was initiated by a private/public consortium (Deichmann et al., 2009). The first fluid injection was performed as an injection test on 23 November 2006. It took 75 hours with the maximum flow rate of 10L/min. According to the interpretation of the hydraulic data, the effective permeability was ~ 0.01 mD under the radial flow condition. In addition, it shows clear indication of the flow dominated by a few fractures (Bourdet, 2002; Häring et al., 2008).

Since 2 December 2006, the hydraulic stimulation was started

and 11570m³ volume of water was injected until 8 December 2006. The maximum flow rate was 55L/s with the wellhead pressure up to 29.6MPa. On the last day of injection, the flow rate was reduced due to the high seismic activity and the well was shut-in at 11:33 on 8 December. After several hours, bleed-off started and total amount of 3400m³ was produced from the well over a 14-month period.

2.2.2. Characteristics of LMEs

In this region, the historical seismicity with the magnitude of M_L 6.5–6.9 occurred in 1356 and moderate seismicity sometimes observed since 1975. (Håring et al., 2008).

During hydraulic stimulation, the seismic rate and magnitude seemed to increase with rising flow rate and pressure. However, during the last stage of injection, the seismic rate reached almost 200 events per hour and M_L 2.6 event occurred at 3:06 on 8 December. According to the traffic light system, the well was shut-in. However, at 5 hours 14 minutes after shut-in, M_L 3.4 earthquake occurred just before starting bleed-off (Mukuhira et al., 2017). Bleed-off was effective to reduce the seismic rate, but several LMEs over magnitude 3 still occurred near to the injection site during the following year (Mukuhira et al., 2013).

By analyzing focal mechanism data, Mukuhira et al. (2017) could find some characteristics of induced seismicity during the shut-in stage. After shut-in, the seismic cloud gradually grew farther and LMEs usually took place at the edge of the seismic cloud. Additionally, the pore pressure decreased as the fluid went farther from the injection point. However, after shut-in, the pore pressure distribution became uniform along the distance from the well (Figure 2.2).

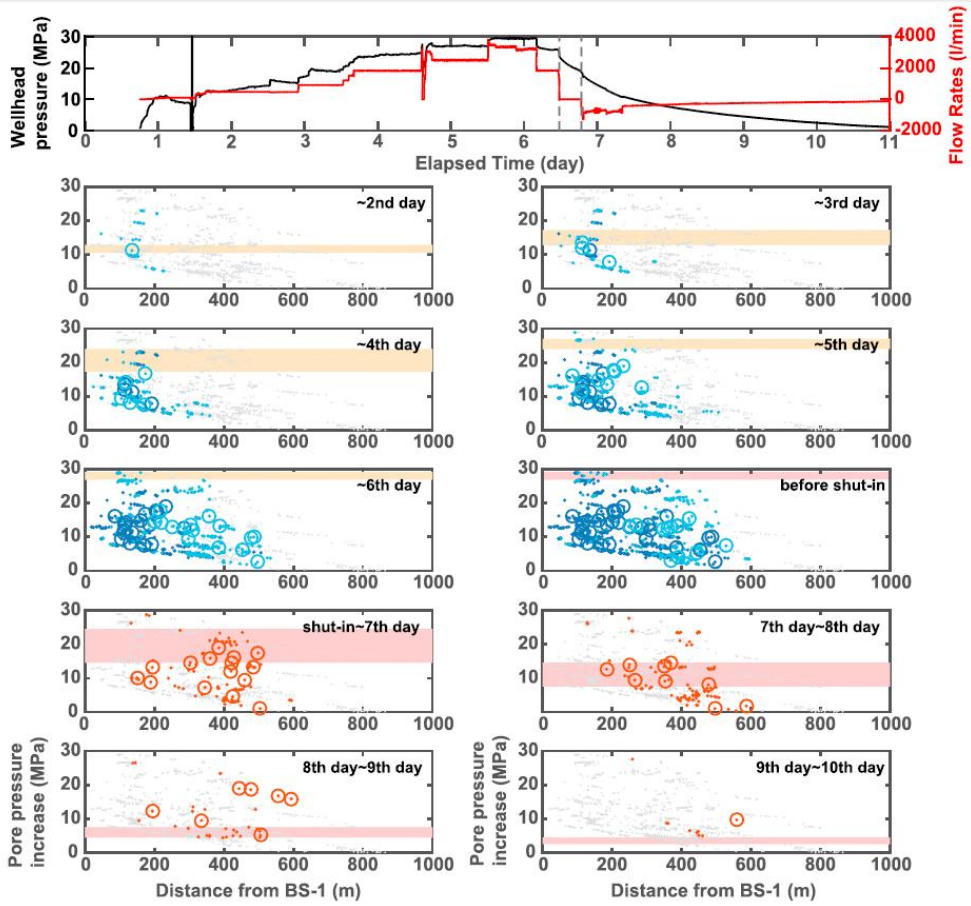


Figure 2.2: Injection history and snapshots of spatial pore pressure distribution in Basel (Mukuhira et al., 2017).

2.2.3. Fault system

The Basel region is in the Upper Rhine Graben, which contains the fault pattern striking NNE, ENE and NW. By the acoustic image logging, fracture set striking NW or NNW was dominant with steep dips. (Häring et al., 2008). After the induced seismicity occurred, the focal mechanism analysis was conducted with the seismic data. According to this analysis, more meaningful data of fault orientation and location were collected and arranged (Kraft et al., 2014; Deichmann et al., 2014; Mukuhira et al., 2017). Figure 2.3 shows the fault system in Basel. All data from Kraft et al. (2014), Deichmann et al. (2014) and Mukuhira et al. (2017), were collected all together. The undetermined actual fault between two nodal planes from focal mechanism data was determined by visual inspection. The red box in Figure 2.3 contained faults near the main shock of $M_L 3.4$ earthquake.

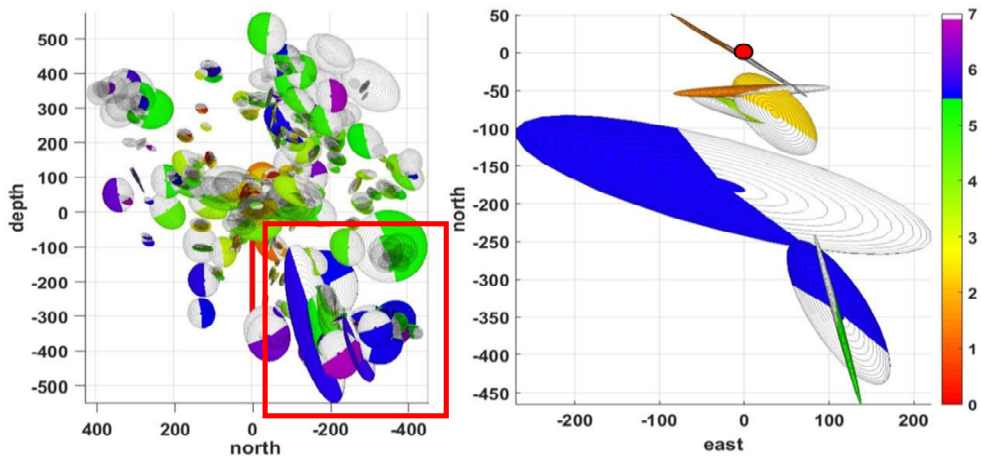


Figure 2.3: (Left) Fracture system in Basel (E-W section view). (Right) Plane view of faults located below the casing shoe and in the south-eastern part in the red box of the left figure. The red dot in the right figure and the red line in the left figure depict the injection hole. (Kraft et al., 2014; Deichmann et al., 2014; Mukuhira et al., 2017)

2.3. Soultz–sous–forêts, France

2.3.1 The brief information of hydraulic stimulation

Before a series of massive fluid injection at 5km depth, some stimulation tests on GPK1 and GPK2 were performed at the 3600–3800m interval until 1997 (Schill et al., 2017). To stimulate the deep reservoir, the massive water volume injected into GPK2, GPK3, and GPK4 until 2005. During this period, some chemical stimulation was also performed, but the injected volume of chemicals is much smaller than hydraulic stimulation. After 2008, circulation experiments were mainly conducted. GPK3 and GPK1 became injection well while GPK2 was producing well and GPK4 was used for both injection and production well (Figure 2.4 and 2.5).

2.3.2 Characteristics of LMEs

The overall characteristics of seismic events in Soultz–sous–forêts were similar to those of Basel. During first stimulation of GPK2 in 2000, the largest earthquake whose magnitude was M_L 2.6 occurred after 10 days of shut–in. The largest magnitude earthquake took place again after shut–in during GPK3 stimulation in 2003. (Figure 2.4) When GPK4 was stimulated first time, the larger magnitude earthquake was also observed during shut–in stage, but this phenomenon did not happen at the second stimulation of GPK4.

Interestingly, several hydraulic stimulations into the similar depth interval were performed in Soultz–sous–forêts, so Kaiser effect was apparent (Baisch et al., 2003). Particularly, GPK4 was stimulated two times, and the seismicity started to occur in second stimulation of GPK4 when the well head pressure exceeds the previous maximum pressure. (Figure 2.4 and 2.5)

According to the analysis of focal mechanism, the tensile rupture was not clearly observed, and shearing the pre–existing

faults was dominant source of seismic events, especially the largest magnitude earthquake. (Charl ty et al, 2007) In addition, earthquakes with the largest magnitude during the hydraulic stimulation in 2003 and 2005 occurred on the intersection of faults.

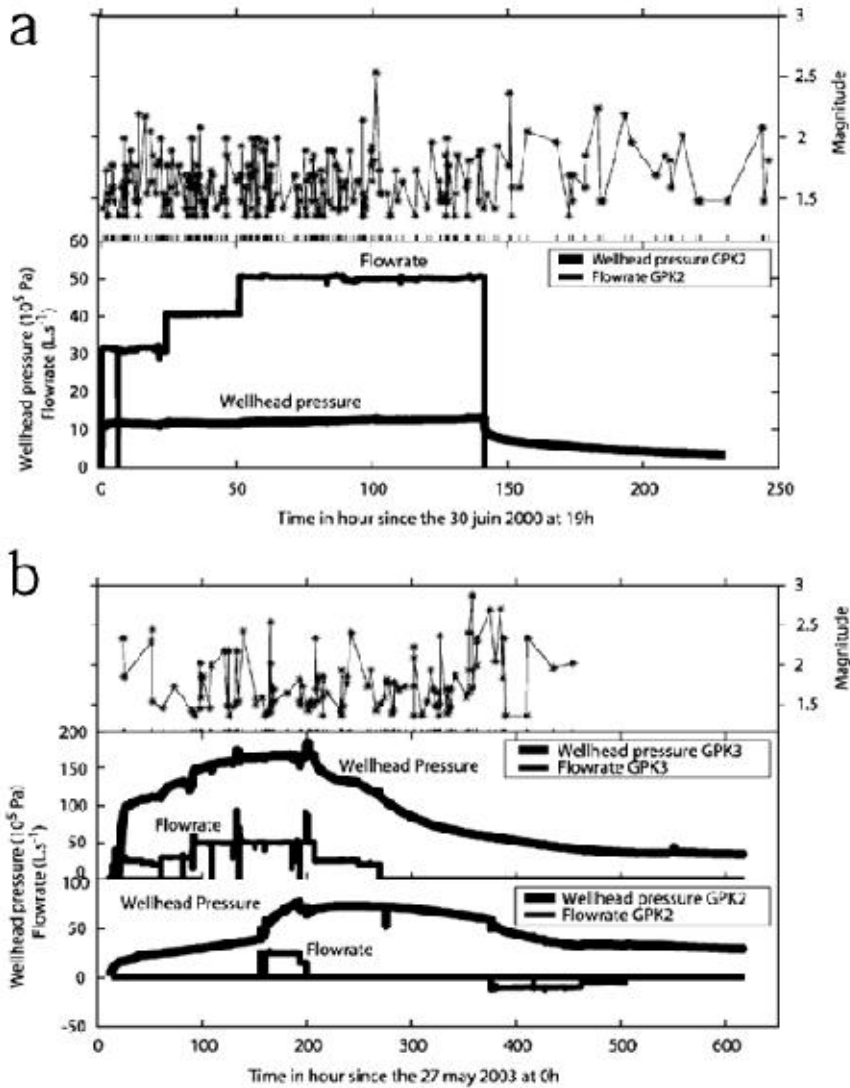


Figure 2.4: (a) (Top) The seismic history of events larger than or equal to 1.4 for GPK2 stimulation in 2000. (Bottom) The injection history of flow rate and wellhead pressure. (b) (Top) The seismic history of events larger than or equal to 1.4 for GPK3 stimulation in 2003. (Bottom) The injection history of flow rate and wellhead pressure (Charl ty et al, 2007).

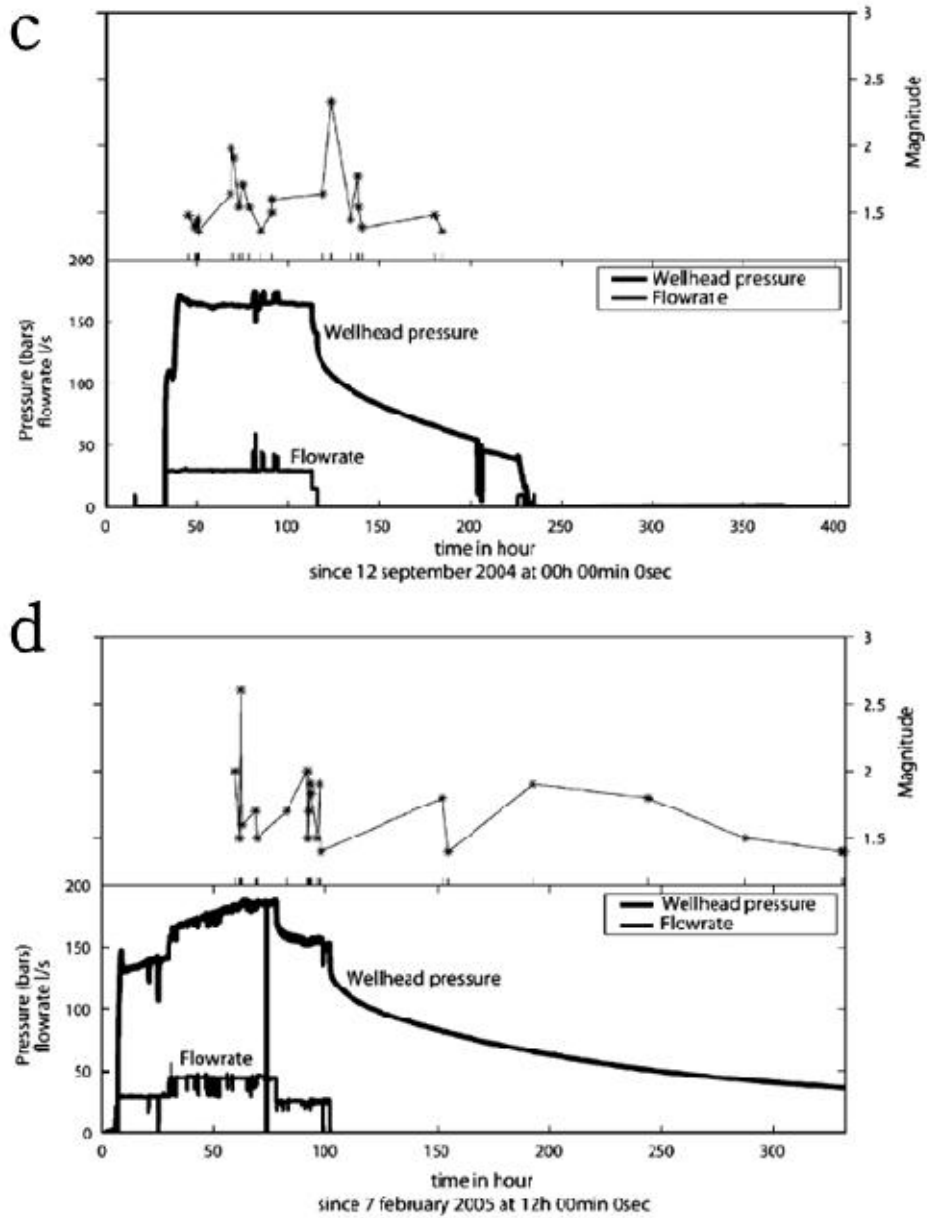


Figure 2.5: (c) (Top) The seismic history of events larger than or equal to 1.4 for GPK4 stimulation in 2004. (Bottom) The injection history of flow rate and wellhead pressure. (d) (Top) The seismic history of events larger than or equal to 1.4 for GPK4 stimulation in 2004. (Bottom) The injection history of flow rate and wellhead pressure(Charl ty et al, 2007).

2.3.3 Fault system

Soultz-sous-forêts is located in the western part of the Upper Rhine Graben and the NNW-SSE striking fracture system is dominant (Kappelmeyer, 1991). To investigate actual fault system, UBI logging data, seismic location data, and VSP data were analyzed comprehensively. Several fracture zones were consistently matched from overall analysis, so total 53 fractures were determined (Sausse et al., 2010).

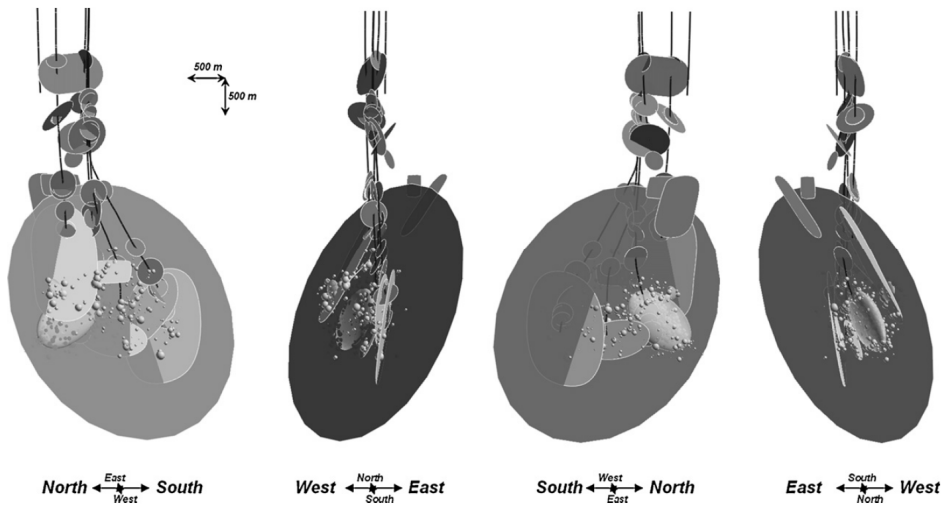


Figure 2.6: 3D views of defined faults in Soultz-sous-forêts (Sausse et al., 2010).

2.4. Cooper Basin, Australia

For the purpose of the geothermal energy development, 6 wells were drilled in the Cooper Basin region. Habanero 1 well was hydraulically stimulated first. Total 34000m^3 of water was injected and M_L 3 earthquake occurred on 14 November 2003 during the shut-in stage after 2000m^3 of water was injected (Asanuma et al., 2005). However, the seismic monitoring system was not close to the site, so the seismic location and cluster gave the limited information about the fault. After Habanero 1 stimulation, Jolokia 1 and Habanero 4 were drilled and stimulated in 2010 and 2012. With only 380m^3 injected water, the largest magnitude earthquake of M_L 1.6 occurred in Jolokia 1 well when 127 days passed after shutting in the well (Baisch et al., 2015).

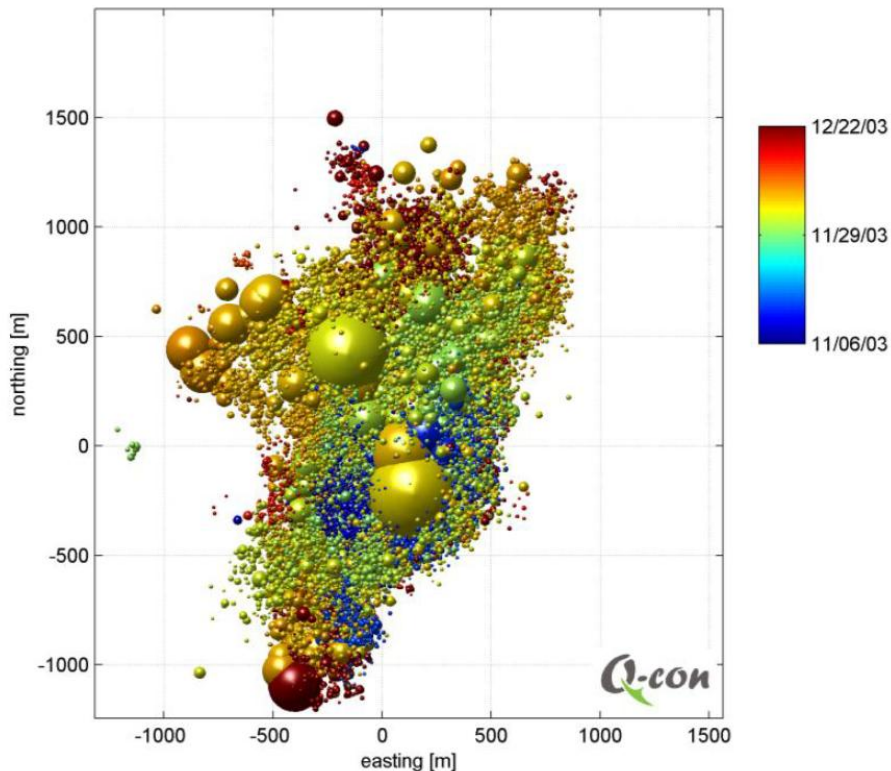


Figure 2.7: Hypocenter locations of seismic events from the 2003 stimulation of Habanero 1. The origin point is the location of Habanero 1 (McMahon et al., 2013).

2.5. Characteristics of LMEs during shut-in stage

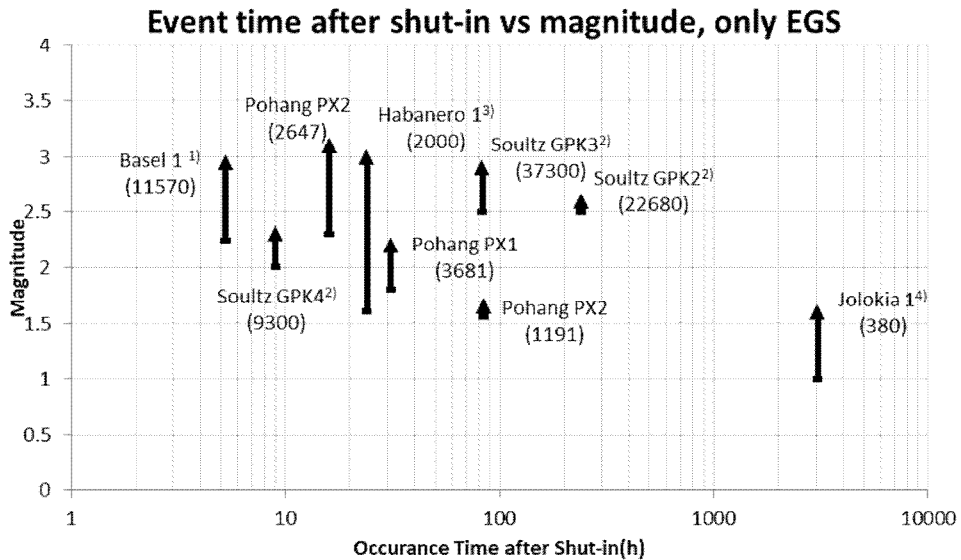


Figure 2.8: The graph of the largest magnitude after shut-in. The start of arrow indicates the largest magnitude during injection, and the end of arrow indicates the largest magnitude during shut-in stage. The number in the bracket indicates the total injected volume(m^3) until each event. 1) : Mukuhira et al.(2017), 2) : Charl  ty et al.(2007), 3) : Asanuma et al.(2005), 4) : Baisch et al.(2015)

Figure 2.8 shows that the magnitude difference between the largest magnitude during injection stage and during shut-in stage has been less than 1.4. According to previous physical studies, the seismicity was contained by the pre-existing fault and the compressive rupture was dominant rather than the tensile rupture.(Deichmann et al., 2009; Charl  ty et al., 2007) While the overall seismicity migrated upward after shut-in, significant LMEs were located both shallow and deep parts. (Schoenball et al., 2013; Mukuhira et al., 2017) The detailed seismic location with well-defined fault system in 5 km depth reservoir was studied in Basel and Soultz-sous-for  ts. According to those data, the faults that contained the largest magnitude earthquakes did not directly meet the injection well except for some events located on the intersection to other fault. Those faults with the largest earthquake

connected with the well by several connecting faults. After shut-in, most seismicity occurs at the periphery of the seismic cloud (Asanuma et al., 2006; Häring et al., 2008; Baisch et al., 2006, 2010; Mukuhira et al., 2016). The largest magnitude of earthquakes seemed to be proportional to the total injected volume regardless of the occurring timing (McGarr et al., 2017).

2.6. Previous studies

Several researches were conducted to clarify the mechanism of LMEs during shut-in stage. Each research used different approach and offered possible explanations on the mechanism.

2.6.1. Pore pressure gradient effect

The pore pressure gradient effect is the mechanism that the lowered pore pressure gradient during shut-in stage can induce more area to slip at once. After shutting in the well, the pore pressure profile along the fault becomes uniform, but the pore pressure at the pressure front still increases. (Figure 2.9) Under the assumption of the uniform critical pore pressure, the lower pressure gradient can make more area to slip with increasing pore pressure over the critical pore pressure (Baisch et al., 2009; Mukuhira et al, 2017).

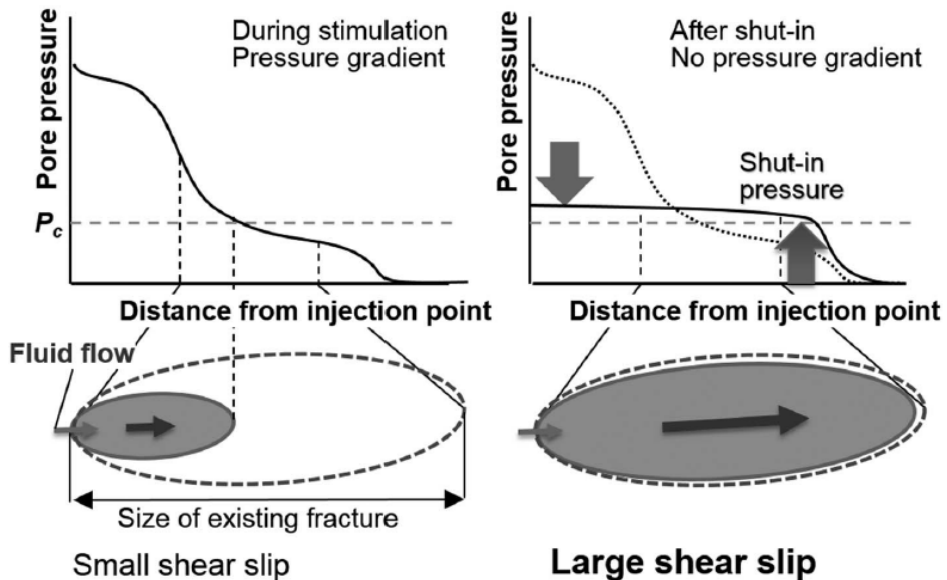


Figure 2.9: Schematic diagram of the mechanism of pore pressure gradient effect (Mukuhira et al, 2017).

2.6.2. Unstable rupture propagation

By fracture mechanics, the largest magnitude earthquake can be explained by the unstable fracture propagation. Galis et al.(2017) modeled the fracture, and applied the background stress drop uniformly with the point load of pore pressure at the center. The magnitude of the largest arrested rupture derived by the fracture mechanics was well matched with the simulation result. By relating the magnitude of the largest arrested rupture with the injected volume of fluid, this paper suggested the new relationship between the maximum moment and the amount of injected fluid. According to this paper, if the condition of the unstable propagation is met, the rupture could propagate unstably within the whole fault regardless of the shut-in.(Figure 2.10)

Norbeck et al.(2018) suggested the condition for the unstable rupture propagation by adopting faulting criterion, $C(= \tau_0 / \sigma_{eff} / f_d)$, where τ_0 and σ_{eff} are the shear and effective normal stresses on the fault, respectively, before the injection and f_d is the dynamic friction coefficient. Based on the several sets of simulations, the point which has the faulting criterion transitions across $C=1$ was well-matched with the rupture arresting location. However, in the case of $C>1$ at the initial state of the fault, the unstable rupture occurs. However, considering the shear dilation, the shear slip decreases the pore pressure instantly and the effective normal stress becomes larger. This phenomenon prevents the unstable rupture and limits the rupture size within several tens of meters.(Figure 2.11)

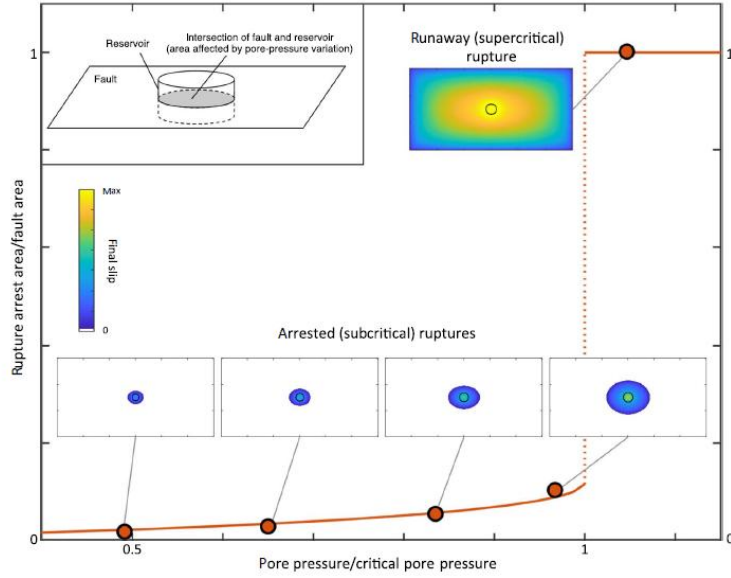


Figure 2.10: The stable and unstable rupture diagram along the pore pressure change (Galis et al., 2017).

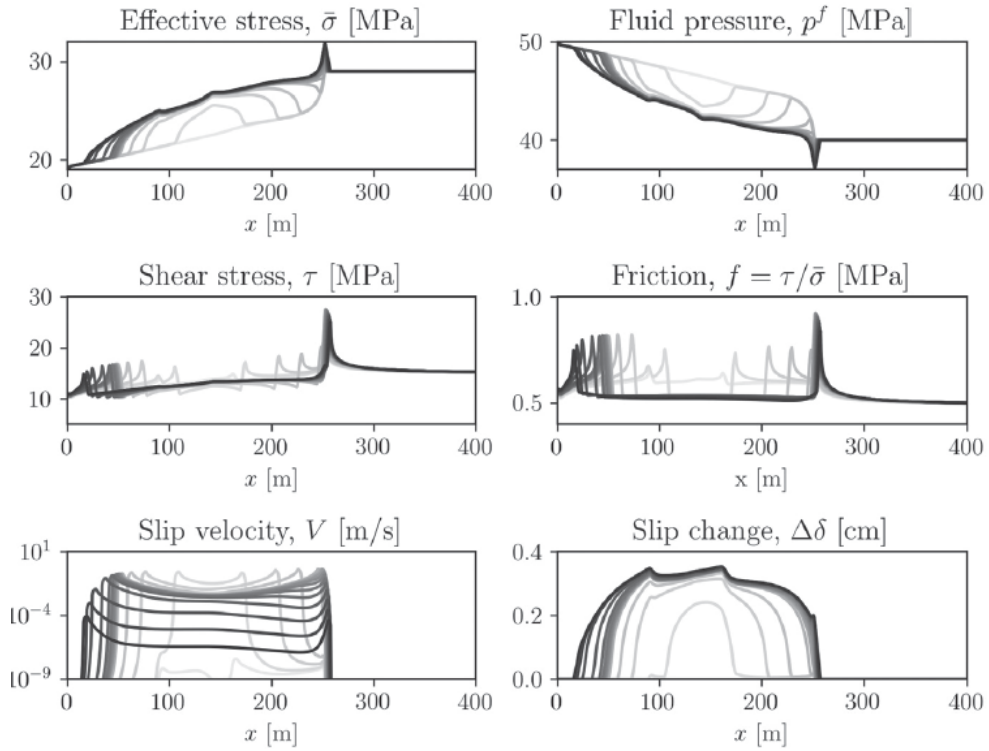


Figure 2.11: The general rupture profile with the shear dilation effect (Norbeck et al., 2018).

2.6.3. Numerical studies

The hydro-mechanical simulation was conducted and showed the effect of the backflow from the several dead-end fractures the well passed. The backflow prevented the sudden drop of the pore pressure around the injection point after shut-in, so the additional moment could occur after shut-in comparing to the total moment of the model without backflow. However, the larger moment of earthquake after shut-in was not shown (McClure, 2015).

The thermo-hydro-mechanical effect was considered by superposing each effect. This research concluded that the poroelastic effect could activate more variously oriented fault after shut-in. While injecting the fluid, the pore pressure builds up along the fault, and it forms high pressure gradient through the matrix. However, after shut-in, the pore pressure drop in the fault causes the uniform pressure distribution to the matrix. By the poroelasticity, the pore pressure gradient through the matrix acts as the body force, so some faults oriented by the specific angle in the matrix are locked during the injection and released after shut-in. Due to more activated faults, the domino effect can occur easily and generate the large magnitude earthquake that could not take place during injection (Simone et al., 2017).

Chapter 3. Semi-analytical approach for magnitude estimation during shut-in stage

3.1. Model description

Pore pressure diffusion was suggested as the mechanism behind the spatio-temporal distribution of microseismicity, and the field-scale hydraulic diffusivity of reservoirs was derived by matching the triggering front with the square-root time relation. This approach is called as seismicity-based reservoir characterization (SBRC) and applied to the hydraulic stimulation data in Fenton Hill and Soultz-Sous-Forêts in 1993 (Shapiro et al., 2002). The SBRC approach was extended to consider the non-linear diffusion by adopting the power-law and exponential dependence of diffusivity on pore pressure (Eq. (3.1)). The triggering front propagates by the square-root temporal dependence in 1D and 2D pore pressure diffusion, but 3D case shows smaller exponent (Hummel and Shapiro, 2012).

$$D_{\text{exp}}(p(r;t)) = D_0 \exp(\kappa p(r;t)) \quad (3.1)$$

$$D_{\text{power}}(p(r;t)) = (n+1)D_0 p(r;t)^n$$

where D : Diffusivity

κ : Permeability Compliance

r : Distance from injection

In this study, a modified diffusion equation instead of Eq. (3.1) is adopted to mimic the non-linear diffusion behavior. The axially symmetric fault was assumed and divided into two parts: stimulated area and unstimulated area. From the injection point to the end of the stimulated area, the larger aperture and smaller joint stiffness than those properties of the outer part were applied. At the boundary between two areas, the continuous pressure and flow rate were adopted as the boundary condition.

$$\begin{aligned}
\frac{\partial^2 p}{\partial r^2} + \frac{1}{r} \frac{\partial p}{\partial r} &= \begin{cases} \frac{1}{c_{v1}} \frac{\partial p}{\partial t} & (0 < r < R) \\ \frac{1}{c_{v2}} \frac{\partial p}{\partial t} & (r > R) \end{cases} \\
r \rightarrow 0 : \frac{2\pi r_w h_1 k_1}{\mu} \frac{\partial p}{\partial r} &= Q \\
r \rightarrow \infty : p &= 0 \\
r \rightarrow R : \begin{cases} \lim_{r \rightarrow R^-} p = \lim_{r \rightarrow R^+} p \\ \frac{2\pi h_1 k_1}{\mu} \frac{\partial p}{\partial r} = \frac{2\pi h_2 k_2}{\mu} \frac{\partial p}{\partial r} \end{cases} \\
k_i = \frac{a_i^2}{12}, \quad h_i = a_i, \quad c_{vi} = \frac{a_i^3 K_n}{12\mu}
\end{aligned} \tag{3.2}$$

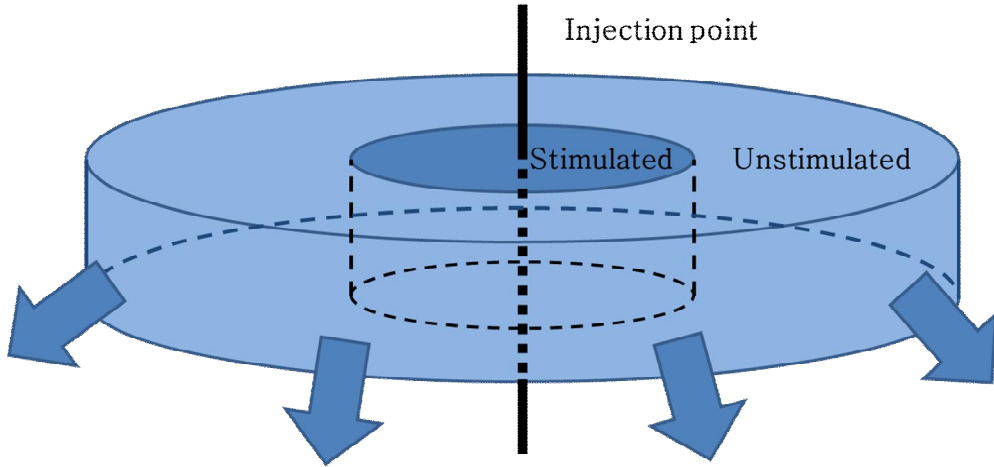


Figure 3.1: The schematic diagram of the semi-analytical model.

K_n is the joint normal stiffness, a is aperture, h is the height of the fracture zone which is assumed to be the same with the aperture, μ is the fluid viscosity, R is the radius of the stimulated area, and Q is the flow rate. I and K below are modified Bessel functions. The equation below shows the Laplace-transformed solution. By applying Talbot's method (Abate & Whitt, 2006), the solution can be numerically inversed.

$$\bar{p}(s, r, R) = \begin{cases} AI_0 \left(r \sqrt{\frac{s}{c_{v1}}} \right) + BK_0 \left(r \sqrt{\frac{s}{c_{v1}}} \right) & (r \leq R) \\ CK_0 \left(r \sqrt{\frac{s}{c_{v2}}} \right) & (r > R) \end{cases} \quad (3.3)$$

$$\text{Let } S_1 = R\sqrt{s/c_{v1}}, \quad S_2 = R\sqrt{s/c_{v2}}$$

$$B = \frac{q\mu}{2\pi h_1 k_1 s} \quad (3.4)$$

$$A = \frac{a_1^3 / a_2^3 \sqrt{c_{v2} / c_{v1}} K_1(S_1) K_0(S_2) - K_0(S_1) K_1(S_2)}{a_1^3 / a_2^3 \sqrt{c_{v2} / c_{v1}} I_1(S_1) K_0(S_2) + I_0(S_1) K_1(S_2)} B$$

$$C = \frac{AI_0(S_1) + BK_0(S_1)}{K_0(S_2)}$$

$$p(t, r, R) = \begin{cases} L^{-1}(\bar{p})(t, r, R) & (t \leq t_{shut}) \\ L^{-1}(\bar{p})(t, r, R) - L^{-1}(\bar{p})(t - t_{shut}, r, R) & (t > t_{shut}) \end{cases} \quad (3.5)$$

To model the transient process, the stimulated area enlarges whenever the periphery of the stimulated area has the larger pore pressure than the upper limit assumed. The increment of the stimulated area was calculated from the periphery of the stimulated area to the place where the pore pressure reached the lower limit. After the stimulated area expanded, the time when the condition of stimulated area expansion was fulfilled was calculated again. This calculating process was consecutively repeated, and the solution for the shut-in case was calculated by superposing the semi-analytical solution of the negative flow rate to the solution of the positive flow rate.

$$t_1 = 0, \quad R_1 = C \quad (C = \text{Constant})$$

Loop

$$\text{Find } t_i : p(R_{i-1}, t_i, R_{i-1}) = P_{\text{upper limit}} \quad (3.5)$$

$$\text{Find } R_i : p(R_i, t_i, R_{i-1}) = P_{\text{lower limit}}$$

end

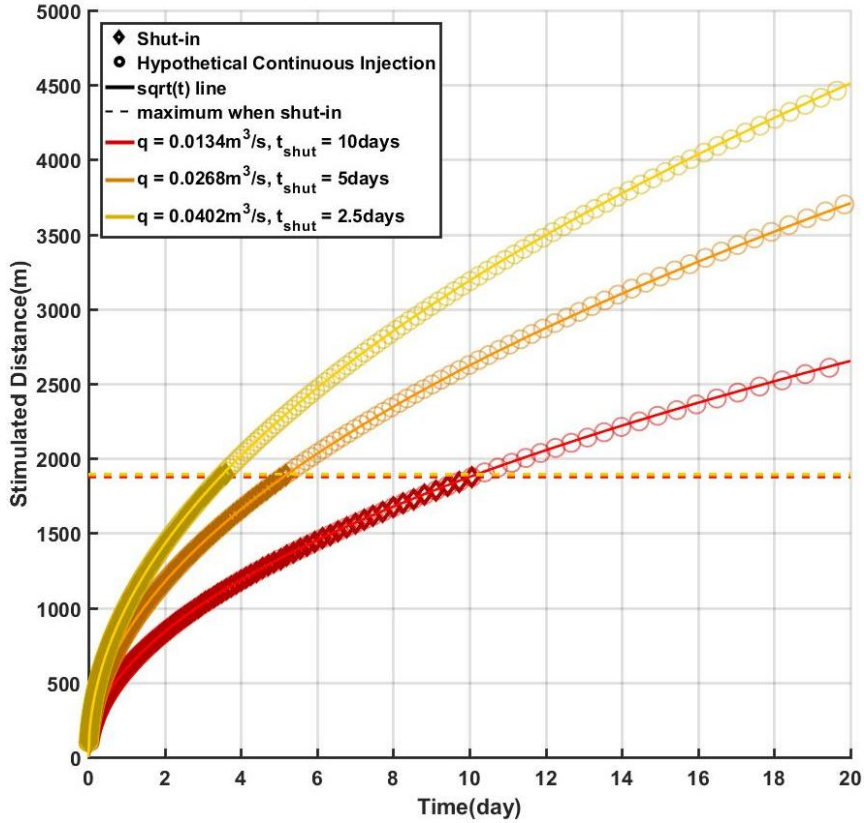


Figure 3.2: The radius histories of stimulated zone for the same injected fluid volume.

This semi-analytical solution can be regarded as the theoretically plausible model describing the pore pressure diffusion in the fracture. Unlike the SBRC approach, the pressure at the triggering front is several mega pascal bigger than zero, but it still follows the characteristics of non-linear 2D diffusion. In Figure 3.2, the radius of stimulated zone corresponds to the triggering front and follows a square-root time dependence. In addition, the maximum triggering front reached during shut-in stage is determined solely by the total injected volume (Shapiro, 2015, Eq. (4.28)).

In this study, this diffusion solution is extended to estimate the magnitude of earthquake. The area exposed to the nearly critical pore pressure ruptures with the onset of slip from the adjacent part at the same moment. To model this rupture propagation, it is

assumed that the area exposed to the certain range of pore pressure is regarded as slipped when the pressure at the adjacent part reaches the critical pore pressure. The possible slip area becomes inversely proportional to the pore pressure gradient. Therefore, the pressure gradient effect can be effectively shown.

To show the trend of the derived solution, parameters estimated from Basel case were used. According to Figure 2.1, the hydraulic stimulation in Basel continued for approximately 5 days with 11570m^3 , so the average flowrate of 26.8L/s was applied. The water dynamic viscosity is assumed as 0.1421cp at reservoir temperature 190°C corresponding to 5000m . (Håring et al., 2008). The aperture at stimulated zone was assumed by matching the maximum pore pressure over hydrostatic pressure as around 30MPa . For estimating the undisturbed aperture, the hydraulic test was conducted before the main hydraulic stimulation, and it resulted in approximately $5\mu\text{m}$ (Håring et al., 2008). However, when this value was applied as the aperture in the unstimulated zone, the pressure decrease at the well during shut-in stage is extremely restricted, so the bigger value was reasonably assumed. This assumption is more realistic because the aperture increase by jacking can take place without shearing and the aperture near to the stimulated boundary affects the diffusion more. The significantly small joint stiffness in the stimulated area was assumed due to considering the shear dilation, but it resulted in the sudden drop of the pore pressure at the injection point when shut-in was done.

This semi-analytic solution has clear limitation. First, this solution does not take into account the dynamic process, such as the pore pressure drop by the dilation, the rupture propagation, and the stress redistribution. Second, the multiple fault system was assumed as single fault and the inhomogeneity of parameters along fault was also ignored. Third, the uniformly distributed aperture within each area makes the pore pressure at the injection point overestimated. However, to overcome those limitations, sensitivity analysis was done. In addition, comparing to the completely uniform

aperture model, this semi-analytic solution can give the better understanding about hydraulic behavior during shut-in stage.

Table 1 Input parameters for semi-analytical solution

Parameters	Unit	Value
Aperture in stimulated zone, a_1	(m)	1.20E-04
Aperture in unstimulated zone, a_2	(m)	3.00E-05
Joint normal stiffness in stimulated zone, K_{n1}	(MPa/m)	1.00E+04
Joint normal stiffness in un stimulated zone, K_{n2}	(MPa/m)	5.00E+05
Viscosity, μ	(cp)	0.1421
Upper limit pressure for slip,	(MPa)	10.0
Lower limit pressure for slip	(MPa)	9.8
Flow rate	(m ³ /s)	2.68E-02
Well radius	(in)	8.5/2
Shut-in moment	(day)	5

3.2. Result

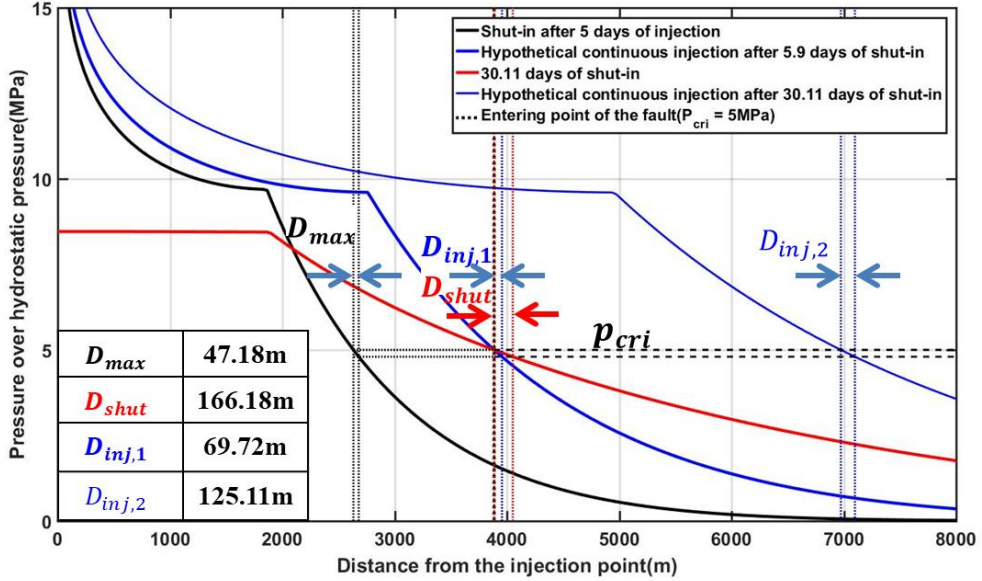


Figure 3.3: The pressure profiles of the semi-analytical solution (Black) at the moment of shut-in, (Red) during shut-in stage, and (Blue) under the condition of no shut-in. (Dashed line) the critical pore pressure interval for determining the possible slip area.

Figure 3.3 shows the general plot generated from the semi-analytical solution. The slip area was considered only at the pressure front because the large seismicity in the field concentrates on the periphery of the seismic cloud and the area stimulated before experiences the stress drop. The largest possible slip area for each moment was measured as the interval where the pore pressure had the value between the upper limit and the lower limit. Due to the assumption of the lowest critical pore pressure of 5MPa, D_{max} is the largest possibly slip area before shut-in. According to Figure 3.3, it is clear that the possible slip area (D_{shut}) during shut-in stage is larger than any other comparable values. ($D_{inj,1}, D_{inj,2}, D_{max}$).

To investigate the magnitude jump during shut-in stage, several kinds of anomalies were assumed to exist and generate LMEs. In this study, the stimulated area expands when the pressure

front reaches 10MPa and 3 kinds of critical pore pressure, 1, 3 and 5 MPa, are assumed as the potential anomaly of this fault system. Those anomalies can be formed by fault interaction, intersection of critically oriented fault, or the heterogeneity of friction coefficient. It is important to point out that those magnitude increases are based on the maximum magnitude at each moment, and no big seismicity can occur if the pressure front fails to meet any of those fault anomalies occupying enough area to slip. In other words, mysteriously sudden increase of magnitude can happen if the pressure front meets the big anomalies with the very low critical pore pressure which does not exist so far. Thus, the actual statistical prediction of large magnitude may need to consider the probability of anomaly' s existence in affected area. For instance, compared to the hypothetical continuous injection, the pressure front propagates slower, but the possible magnitude increases more. In this study, the maximum value of the possible earthquake is analyzed physically not statistically. In addition, even if every LMEs are calculated at the unstimulated area which seemed to exist out of the triggering front in $r-t$ plot of the SBRC approach, the current semi-analytical result is still meaningful in that the field observation is based on the direct distance from the well without consideration of actual flow path.

The magnitude difference was calculated based on the area difference. There were two different relationships between the moment magnitude and the fault length.(Kanamori and Anderson, 1975; Ishida, 1974) In this study, $M_w \sim 2/3 \log(L^2)$ was adopted because the magnitude scale is much less than magnitude 6 and this relationship is more physically plausible if the shear dilation effect on the pore pressure drop is dominantly acted as restraint of rupture propagation. Also, the effect of shear stress on the magnitude was ignored because actual shear stress ratio against the maximum shear stress acting on faults was over 0.3(Terakawa et al., 2012). Compared to the effect of slipped area, this amount of difference among LMEs in Basel was insignificant for the magnitude

jump due to the logarithm in magnitude calculation.

According to Figure 3.4, the aperture in the unstimulated area affects the shut-in behavior significantly. As the unstimulated aperture becomes bigger, the possible magnitude difference rises faster, but it ends sooner after shut-in. The effect of the aperture in the stimulated area is plotted in Figure 3.5. In cases of 150 and 225 micro meters as the aperture in the stimulated area, results were similar comparing to 75 micro meter case. This was because the system becomes highly non-linear while 75 micro meter case is more likely to the linear system. Besides, the aperture within the stimulated area affects the injectivity largely, but has little impact on the shut-in behavior. Thus, the properties of the unstimulated area are more important for the shut-in behavior than the properties of the stimulated area. Interestingly, Figure 3.6 shows that the occurrence time and the magnitude of the largest earthquake is consistent when the total injected volume of fluid is same. This trend is caused by high non-linearity making the unstimulated area as relatively impervious area. Because the higher flow rate ends earlier with the constant injected volume, the magnitude difference becomes larger and takes more time. Therefore, the maximum magnitude and the timing are largely dependent on the total injected volume and the fault properties, especially for the unstimulated area.

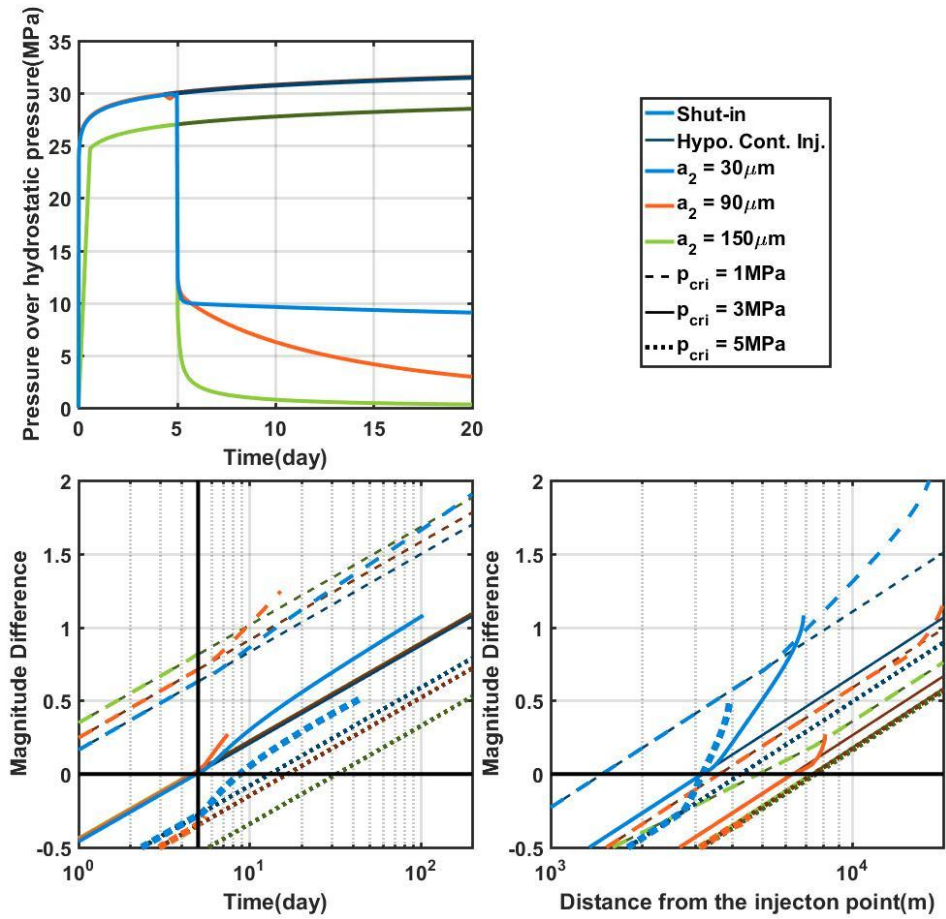


Figure 3.4: (Top Left) The histories of the pore pressure over the hydrostatic pressure at the injection point. (Bottom Left) The possible magnitude jump history with the black vertical line indicating the shut-in moment. (Bottom Right) The possible magnitude jump profile. The possible magnitude jump is calculated based on the maximum possible slip area before shut-in at each case. Different apertures in the unstimulated area were applied in each case.

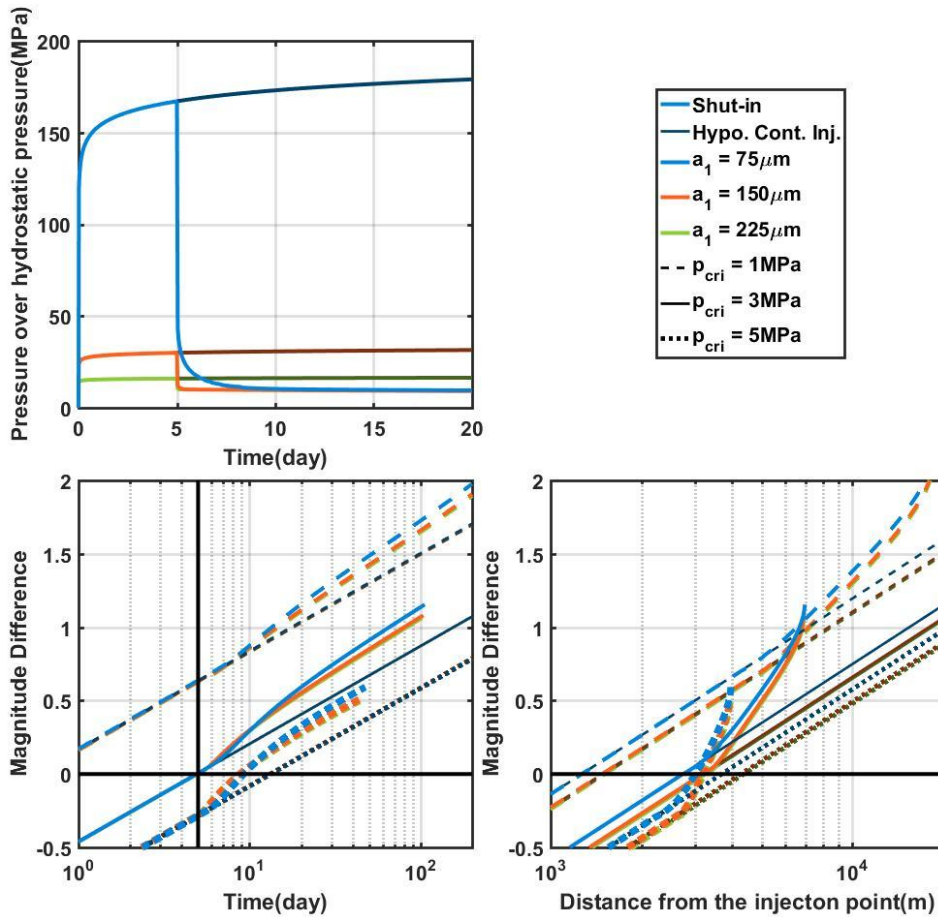


Figure 3.5: (Top Left) The histories of the pore pressure over the hydrostatic pressure at the injection well. (Bottom Left) The possible magnitude jump history with the black vertical line indicating the shut-in moment. (Bottom Right) The possible magnitude jump profile. The possible magnitude jump is calculated based on the maximum possible slip area before shut-in at each case. Different apertures in the stimulated area were applied in each case.

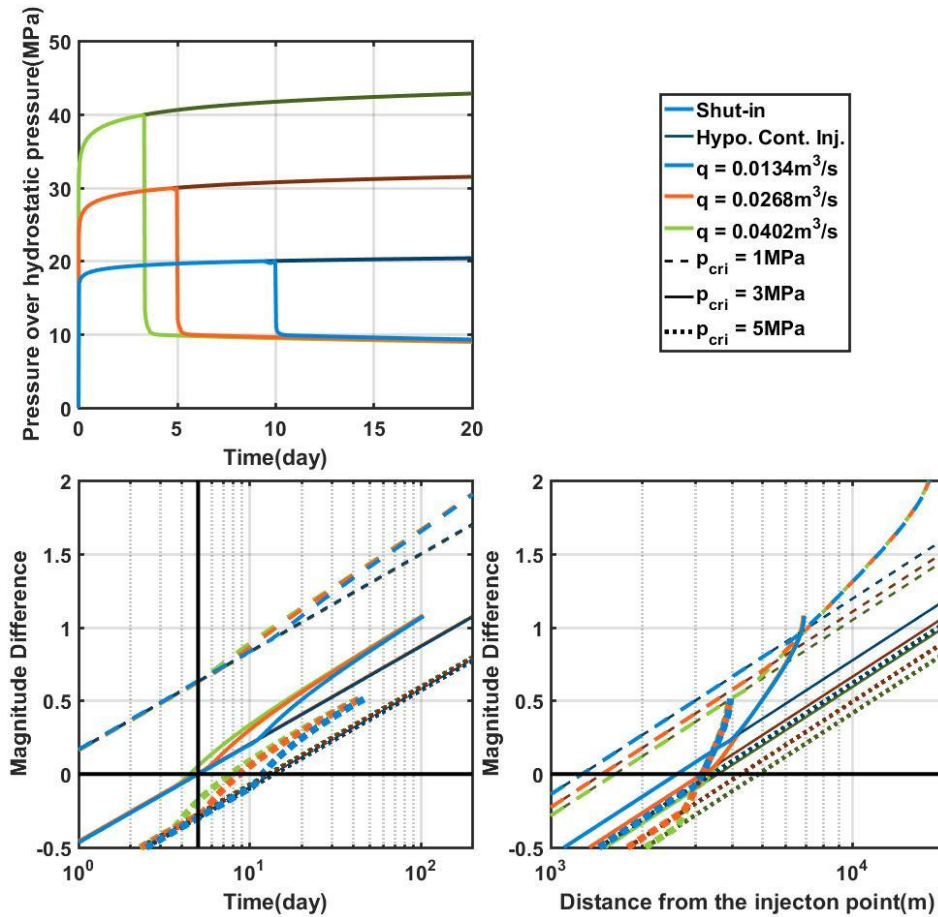


Figure 3.6: (Top Left) The histories of the pore pressure over the hydrostatic pressure at the injection well. (Bottom Left) The possible magnitude jump history with the black vertical line indicating the shut-in moment. (Bottom Right) The possible magnitude jump profile. The possible magnitude jump is calculated based on the maximum possible slip area before shut-in at $0.0268 \text{ m}^3/\text{s}$ case because the fault properties are same. Different flow rate and injection period to conserve the total injected volume are applied in each case.

To conclude, the higher possibility of the larger magnitude earthquake after shut-in is analytically shown and parameters that can affect shut-in behavior are analyzed. The important assumption behind the result is the existence of the sufficiently big anomaly with the low critical pore pressure locating in the unstimulated area, and its critical pore pressure should be lower than the pressure at the boundary of the stimulated area. Unless the anomaly with low critical pore pressure is big enough, the magnitude is limited by the size of anomaly. The basis of this whole analyzed mechanism above can be summarized as the pressure gradient effect, so this effect can be regarded as one of the main mechanisms for the larger magnitude earthquake during shut-in stage. However, this semi-analytical approach modeled the rupture propagation in too simple way calculating the area in the certain pressure range. In addition, this approach ignored the interaction of fault. Therefore, the comprehensive simulation is necessary to analyze the occurrence of the largest magnitude earthquake during shut-in stage.

Chapter 4. Numerical simulation for hydro-mechanical analysis of induced seismicity

4.1. Description of numerical code, UDEC

Universal Distinct Element Code(UDEC) is two-dimensional distinct element method(DEM) simulation tool developed by Itasca(Itasca, 2011). To simulate the fracture flow, the impervious rock mass was assumed and the flow through fracture follows the Cubic' s law. The time-dependent simulation in UDEC is basically quasi-static, so the dynamic effect is ignored. The fault model is stick-slip model that assumes the static and dynamic friction coefficient. To determine the seismicity apart from the aseismic slip, the minimum shear velocity to determine the slip as the seismic event was set as $10 \mu\text{m/s}$. In this study, the joint normal stiffness is assumed to be proportional to the effective normal stress, so the exponential relation between the normal displacement and the normal stress is adopted(Zangerl et al., 2008). However, this relation was discretized due to too high numerical expense for the exponential relationship in the simulation.

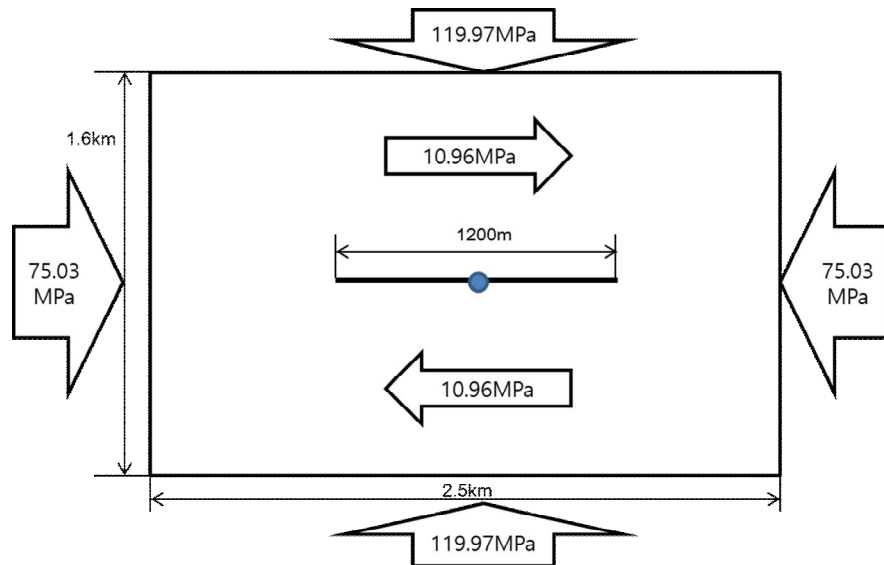


Figure 4.1: The schematic diagram for single fracture simulation.

4.2. Stress redistribution on the single fault

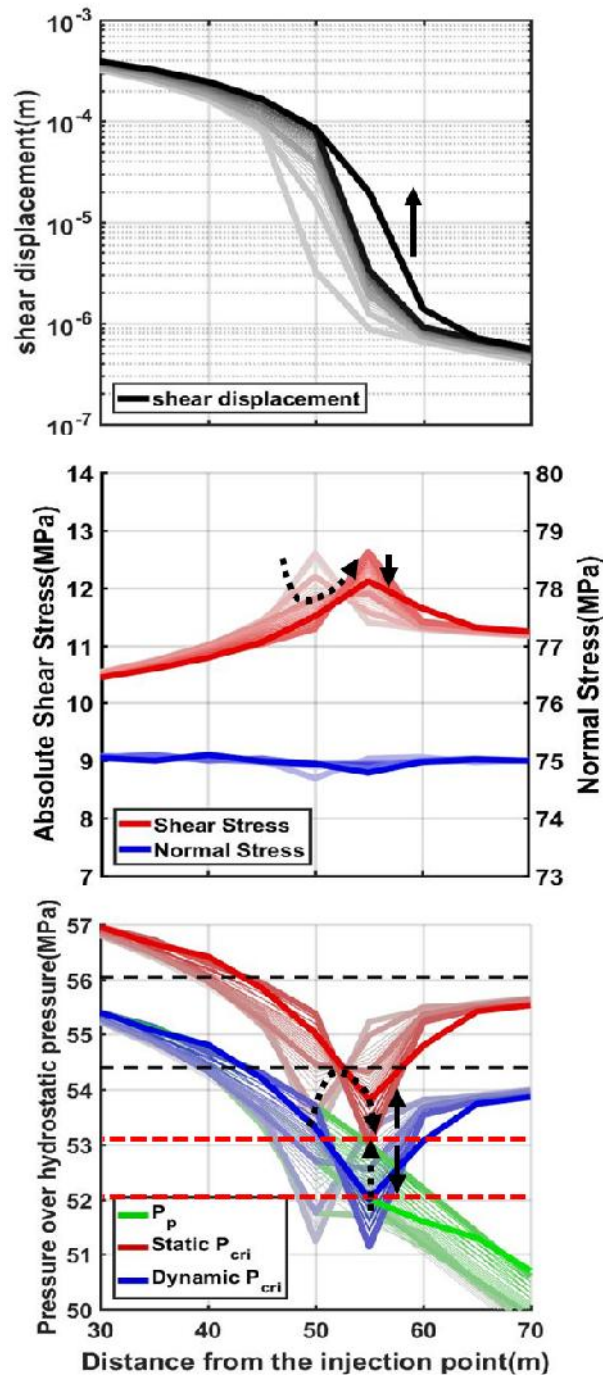


Figure 4.2: The UDEC simulation of shear slip. (Top) The shear displacement profiles around the slipping moment. (Middle) The shear stress and normal stress profiles around the slipping moment. (Bottom) The critical pore pressure and pore pressure profiles around the slipping moment. The time difference between the adjacent thin line is 1.7s and every 5th line is thickened. The passage of time is indicated by the brightness of the color.

Figure 4.2 shows the state around the moment of slip. Two dashed black lines show the static critical pore pressure and dynamic critical pore pressure, respectively, before the stresses are redistributed, and two dashed red lines means those values after the stress redistribution. Dotted arrows represent the direction of temporal change, and solid arrows represent the instant change at the exact moment of slip. As arrows indicate, the shear stress is suddenly released and the pore pressure drops immediately to the dynamic critical pore pressure when the pore pressure meets the static critical pore pressure. Because the slip near the injection point continuously occurs as the fluid injection continues, the shear stress next to the stress-released area was concentrated sequentially.

Once the rupture occurred on the single fault, the stress around the slipped area changes significantly. Under the condition of continuous propagation of pore pressure, the shear stress at the edge of slip area increases because of the continuous slippage by the pore pressure increase on the area slipped before. After the shear stress concentrated on the edge and the pore pressure built up enough to meet the lowered critical pore pressure, the rupture takes place in the limited area where the shear stress is concentrated. At that moment, the pore pressure decreases instantly and the concentrated shear stress releases. In the view of the critical pore pressure, the dynamic critical pore pressure increases at the rupture moment, so the slippage can stop fast. The pore pressure builds up again in the slipped area, and the consecutive small slip occurs.

In conclusion, the simultaneous slip of large area is unlikely to occur in the single fault system. Except the first moment when no stress redistribution by slip occurs, the continuous pore pressure build up leads to the concentrated shear stress at the boundary of the slipped area, and it results in the localized slip. Even in the fault critically oriented, the extensive rupture propagation is prevented by the shear dilation(Norbeck et al., 2018). Especially for the simulation, the anomaly of the low critical pore pressure cannot

exist in the unstimulated area in that the homogeneous fault was assumed and the concentrated shear stress makes the local minimum of critical pore pressure at the front of fluid pressure propagation. Therefore, this study assumed the multi-fracture model to make the anomaly where has the lower critical pore pressure than the reduced critical pore pressure by continuous slip

4.3. Stress redistribution on the multi fracture

Due to the slip on the fault, the stress on other faults is redistributed. This causes Coulomb Failure Stress(CFS) change, which theoretically induces the physical instability, so analyzing CFS has been one of the ways to study the occurrence of aftershocks.(Harris, 1998) Figure 4.5–7 show how CFS changes by the slip–induced stress redistribution. The traditional CFS analysis is that negative ΔCFS means the stabilization and less possibility of slip and vice versa for the positive ΔCFS . Equation 4.1 shows the relationship between CFS and critical pore pressure.

$$\begin{aligned} CFS &= \tau_0 - \mu_s \sigma_{n,eff} \\ \Delta CFS &= \Delta \tau_0 - \mu_s (\Delta \sigma_n - \Delta p_p) \\ &= -\mu_s (\Delta p_{cri} - \Delta p_p) \end{aligned} \quad (4.1)$$

where τ : shear stress

σ_n : normal stress

The important thing is that a lot of shearing preceded the largest magnitude earthquake in the field, so the largest magnitude earthquake can be the result of the stress redistributed by previous shearing including seismic and aseismic slips. Among many slips, the slips on the closest fault or the directly connected fault can be assumed to mainly affect the fault' s stability. Under this assumption, the spatial relationship between two faults can be the factor of determining whether the fault can slip with the large area. In the case of A–2, 3 and B–1,3 in Figure 4.2, ΔCFS shows high positive value but in a very narrow area. This kind of profiles can correspond to the profile on slipping single fault, and the similar mechanism leads to the consecutive but small slips. Because the moment of earthquake is the product of area and shear displacement, small slipped area leads to the small magnitude of the earthquake. On the contrary, the other case, A–1 and B–2, demonstrates the stabilization of the fault, but more area can be

slipped at once if the pore pressure builds up enough to reach the critical pore pressure.

In view of normal and shear stress change, Figure 4.5–4.7 give examples of how those CFS distributions in Figure 4.4 were derived. According to Equation 4.1, the normal stress was reflected in CFS change by multiplying the friction coefficient while the shear stress was not. Thus, the shear stress distribution generally has the dominant effect on both CFS and critical pore pressure distributions. In case of A–1 including the fault oriented 30 degrees (Figure 4.5), the hypothetical faults are stabilized due to the release of shear stress on the slipped fault. However, as the fault orients similar to the perpendicular line of the slipped fault (Figure 4.6), the normal stress change becomes much bigger than the shear stress change near the slipped fault. The intersection point A is located in the part where the normal stress of this case reduces, so the hypothetical faults of A–2 case is destabilized very near the intersection point. A–3 case shows typical stress concentration by shearing because hypothetical faults are placed in the direction similar to the slipped fault. As a result, the localized destabilization near the intersection point is achieved.

This relationship between the spatial relations of connected faults and the magnitude of earthquake is consistent with the result of semi-analytical approach. A–2, 3 and B–1,3 cases can generate the low critical pore pressure anomaly in the unstimulated area, but the anomaly is too small to contain the expected maximum slippage at every moment. However, in A–1 and B–2 cases, the following area next to the intersection point can be regarded as the sufficiently big anomalies of low critical pore pressure comparing to the pressure at the intersection point, which can generate the expected maximum slip. Therefore, the stress redistribution by the slip can be the important factor determining the possibility of the large magnitude earthquake occurrence during shut-in stage.

However, the possibility of simultaneous slip of connected faults cannot be ignored. A–3 and B–1 can indicate the case of slip on the connected fault at the same moment when the previous fault

is slipped. It can be understood as the behavior acting like one fault because faults in A-3 and B-1 are similarly oriented and connected. However, this mechanism has some limitations to explain the occurrence of the largest magnitude earthquake during shut-in stage. First, physically, the slip on the previous fault should be limited to the small amount until the sufficient pore pressure builds up in the connected fault. As shown in Figure 4.2, the slip on the preceding fault leads to the localized instability on the next fault and reduces the possibility of the magnitude increase. Thus, the large magnitude by simultaneous slip can happen only when it is hardly that the preceding fault slips. For this condition, very gentle pore pressure gradient is necessary, which necessitates very low critical pore pressure of those faults and long distance from the injection point. Second, the faulting direction of two faults should be similar. In 3D problem, a little difference of the orientation can result in the significantly different slip direction of faults. Third, in the numerical aspect, the current numerical tool is for 2D problem which exaggerates the pore pressure gradient at the front. Therefore, this effect is physically special case and numerically hard to be shown in the injection-induced seismicity problem, so this study excluded that case.

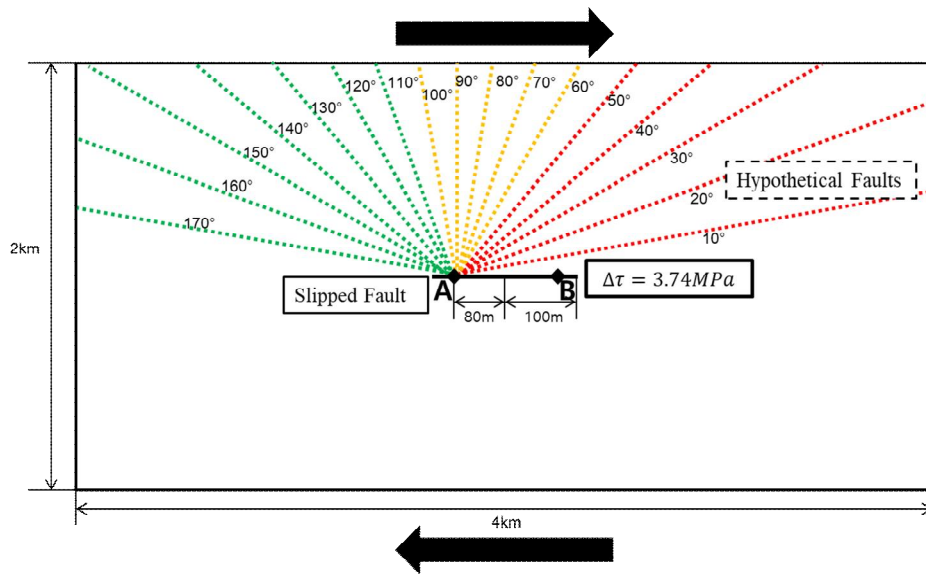


Figure 4.3: Model for shear slip simulation. Uniformly distributed pore pressure is given in the fault centered in the model, and induced the slip.

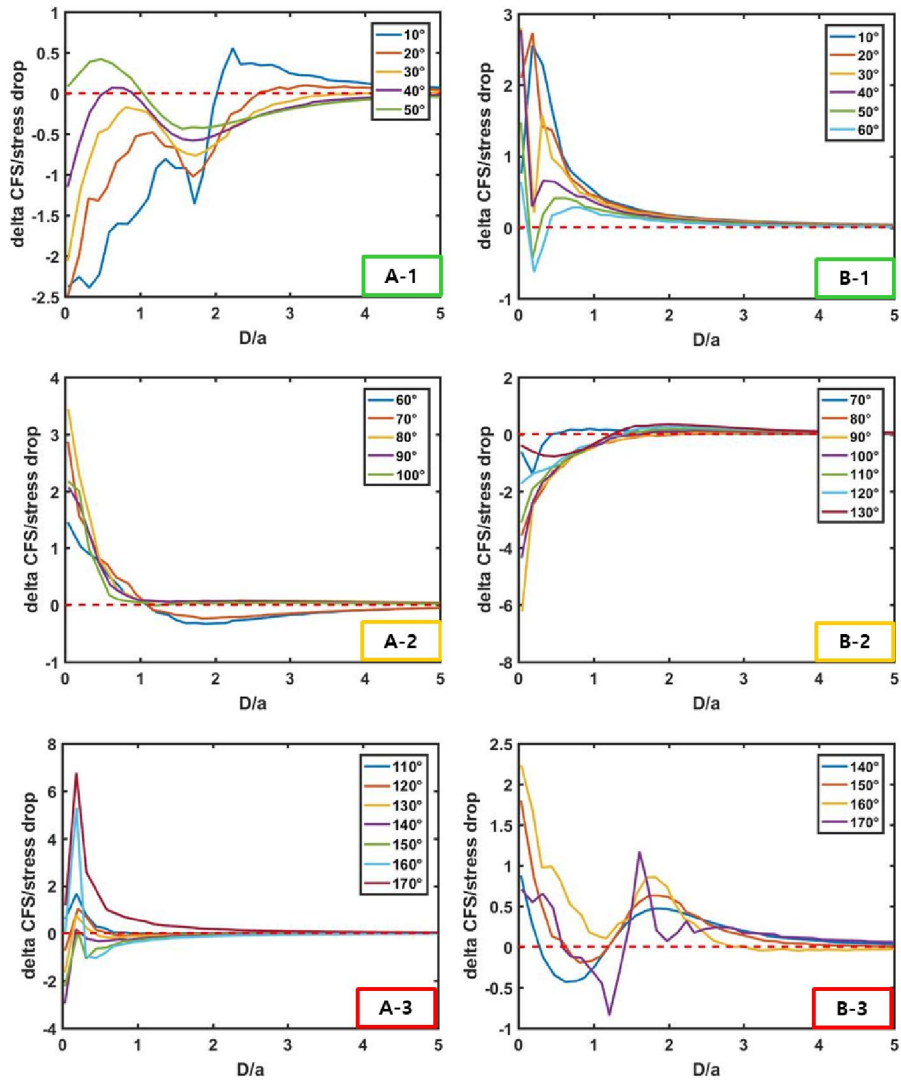


Figure 4.4: Δ CFS profiles normalized by stress drop along each hypothetical fault. A-1,2,3 are profiles from the fault group starting from point A. B-1,2,3 are profiles from the fault group starting from point B. D is the distance from the intersection point(A or B). Each axis is normalized by the stress drop and the half length of fault respectively.

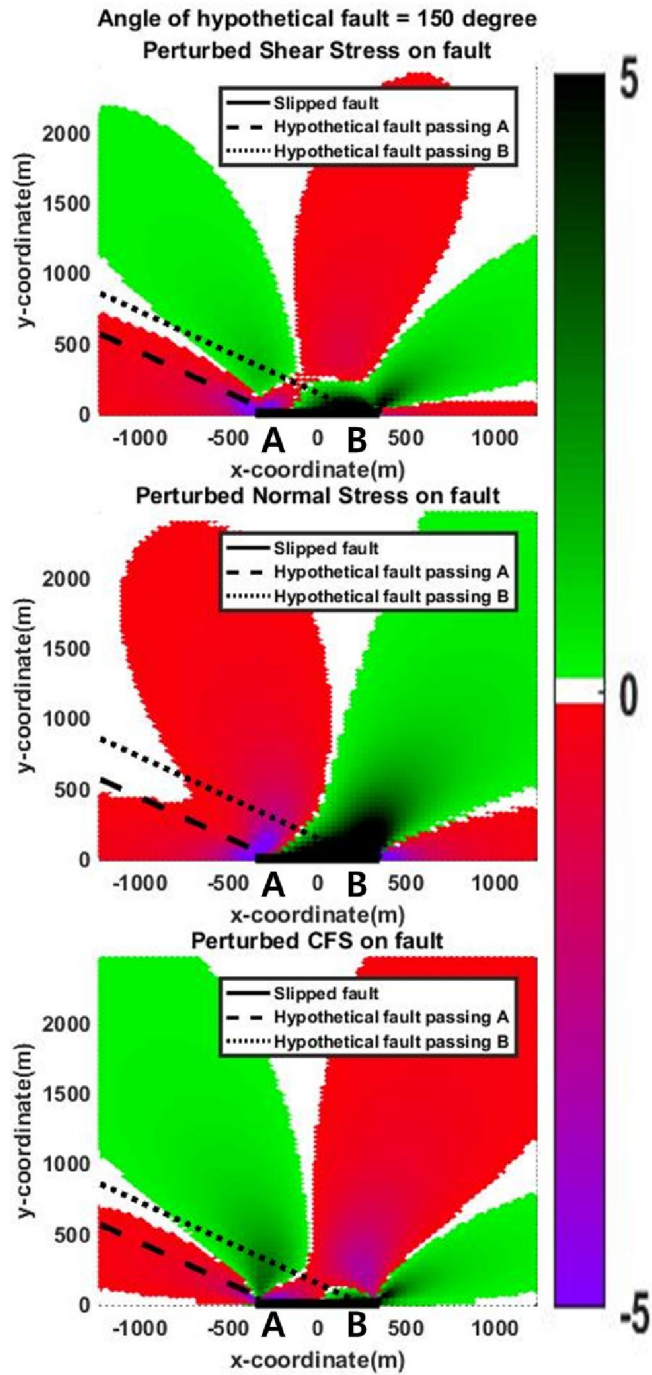


Figure 4.5: Stress change on the direction of the hypothetical fault(Case A-1,B-1).

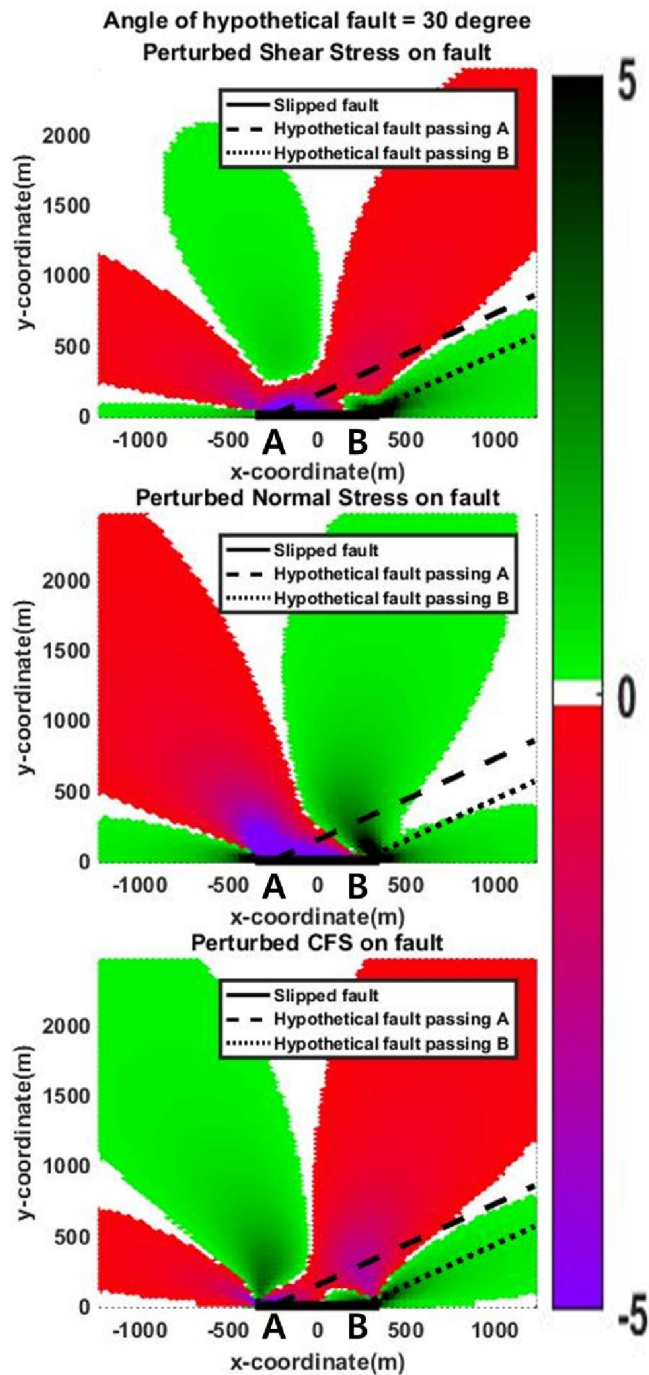


Figure 4.6: Stress change on the direction of the hypothetical fault(Case A-2, B-2).

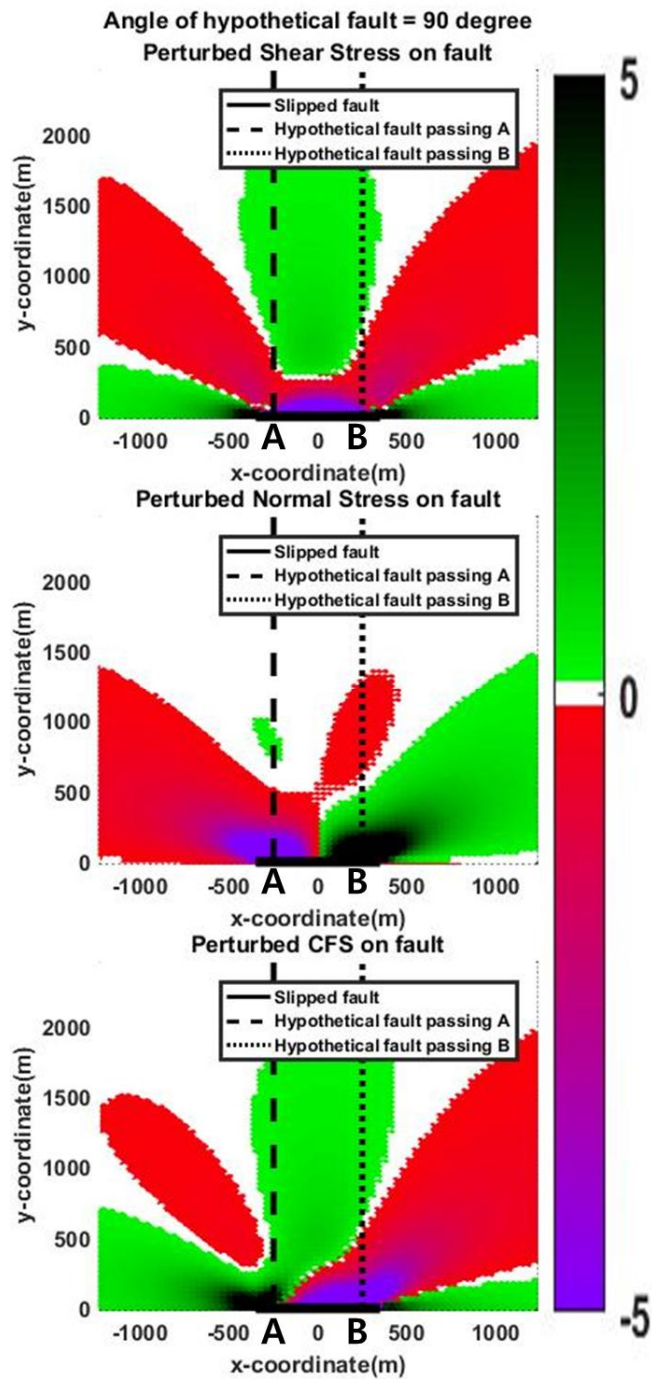


Figure 4.7: Stress change on the direction of the hypothetical fault(Case A-3, B-3).

4.4. Application to Basel case

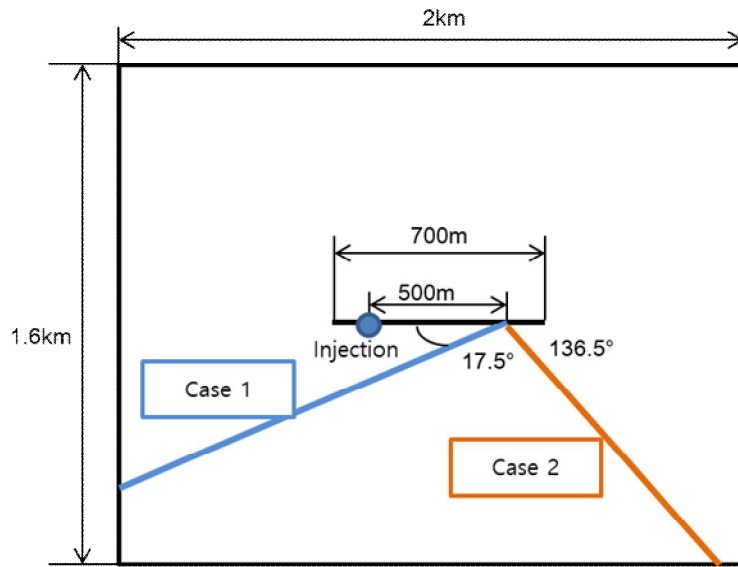


Figure 4.8: Simplified fault system in Basel.

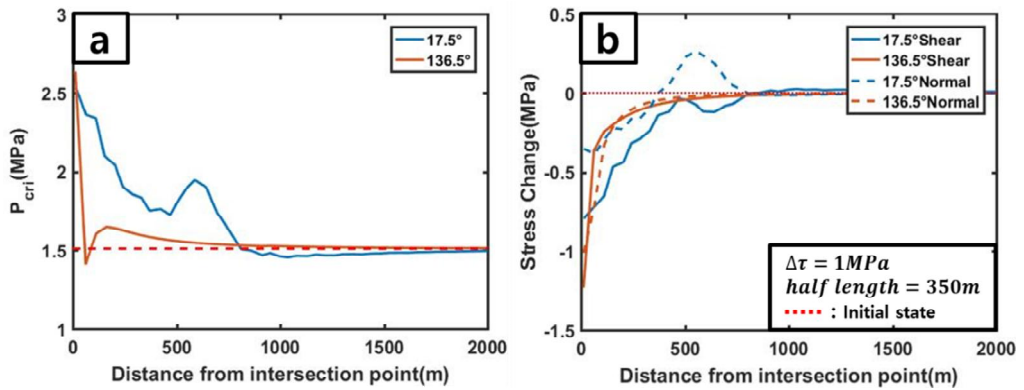


Figure 4.9: (Left) The critical pore pressure profiles and (Right) the normal and shear stress change profiles on the connected faults in both cases .

Table 2 Input parameters for UDEC simulation.

Parameters	Unit	Value	
flow rate, q	($m^3/s/m$)	$3.333333E-5$	
residual hydraulic aperture, a_{min}	(m)	$1.00E-06$	
maximum hydraulic aperture, a_{max}	(m)	$1.20E-04$	
Aperture at zero normal stress, a_0	(m)	$1.20E-04$	
Viscosity, μ	(cp)	0.1421	
dilation angle, φ	($^\circ$)	5	
static friction angle, θ_s	($^\circ$)	30	
dynamic friction angle, θ_d	($^\circ$)	28	
Cohesion, c	(MPa)	0	
stiffness characteristics	$dk_n/d\sigma'_n$	50000	
minimum shear velocity, v_{min}	(m/s)	$1.00E-05$	
Open hole length, L	(m)	400m	
Boundary stress	σ_{xx}	(MPa)	119.97
	σ_{yy}	(MPa)	75.03
	σ_{xy}	(MPa)	10.9593
Initial pore pressure	p_0	(MPa)	46
	σ_1	(MPa)	122.5
Principle stress	σ_2	(MPa)	72.5
	θ_{SHmax}	($^\circ$)	137

*Compression is positive

Figure 4.8 shows the basal fault system based on Figure 2.3. For the simplicity, the fault containing the injection well and the fault of M_L 3.4 event were remained. The flow rate used in the simulation is smaller than the actual flow rate in that the flow rate far from the injection is overly considered due to 2D simulation. Other parameters followed the reported value.

The case 2 was designed to depict the different effect of fault interaction under the certain critical pore pressure same with the case 1. According to Figure 4.9, shearing on the slipped fault in case 1 is expected to stabilize the connected fault while case 2 would induce the localized destabilization of the connected fault.

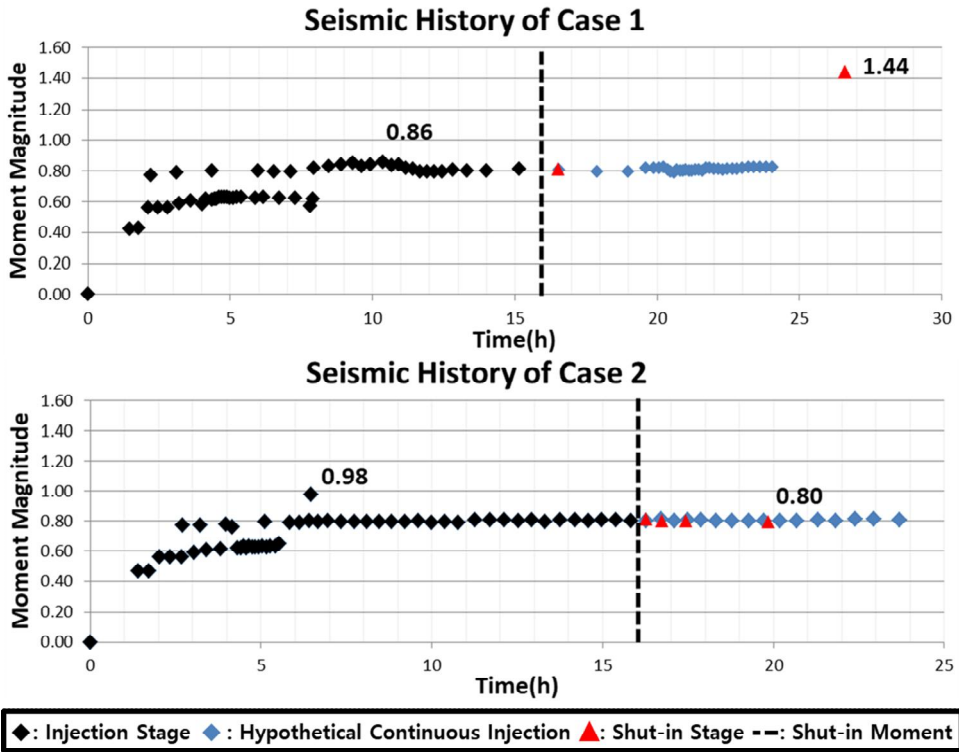


Figure 4.10: Seismic histories of case 1 and 2.

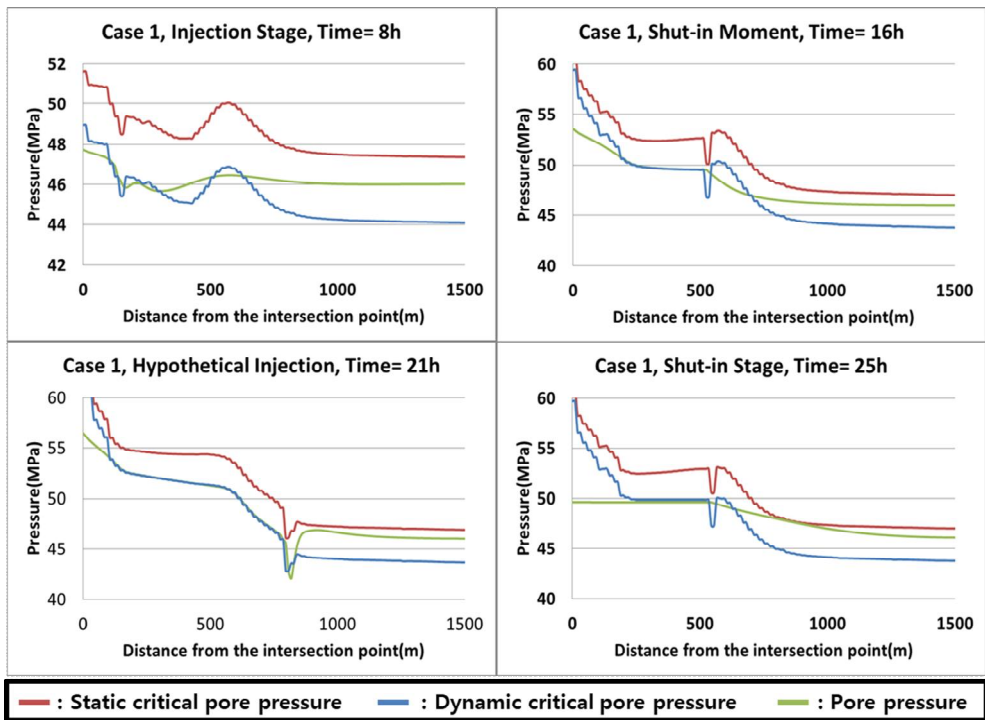


Figure 4.11: Pressure profiles along the connected fault in Case 1.

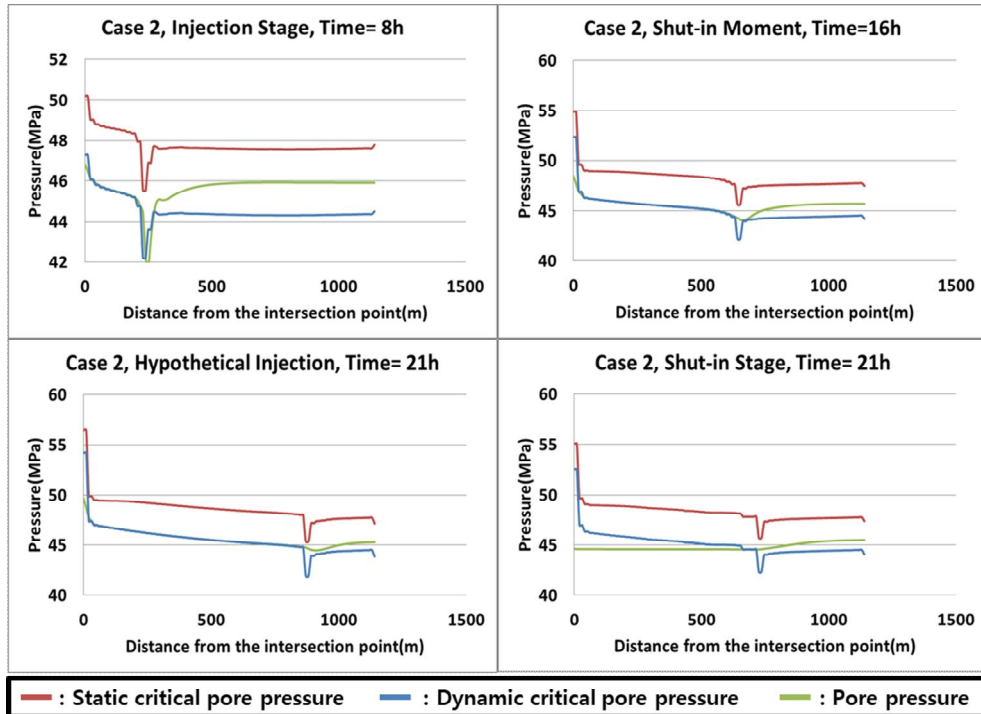


Figure 4.12 Pressure profiles along the connected fault in Case 2.

The largest magnitude earthquake during shut-in stage is only observed in Case 1's shut-in stage. According to Figure 4.10, the magnitude jump was around 0.58, and the location of the largest magnitude event was on the connected fault representing the actual fault contained the largest magnitude earthquake. The location of the earthquake is also near the actual field observation. Additionally, the pressure gradient effect was clearly shown in Figure 4.11.

Also, there are several meaningful results. Without the consideration of fault interaction, both Case 1 and 2 should show the shut-in behavior because the intersected fault has sufficiently small critical pore pressure of 1.5MPa. However, the stress redistribution changed the critical pore pressure profiles. The local minimum value of static critical pore pressure generated by continuous shearing limited the pore pressure at the pressure front, but this local minimum value in Case 1 was larger than static critical pressure out of the pressure front while this value in Case 2 was not. This condition can be regarded as the existence of the low critical pore pressure anomaly in the unstimulated area, so the LME

could occur in Case 1 as expected by semi-analytic approach. On the contrary, Case 2 failed to fulfill the given condition, so the large magnitude earthquake during shut-in stage could not be observed. Therefore, in order to observe the large magnitude earthquake, the sufficient area in the unstimulated area should have the critical pore pressure lower than the lowered critical pore pressure at the pressure front.

Interestingly, the hypothetical continuous injection in Case 1 also failed to generate the large magnitude earthquake. This is because the high gradient at the pressure front prevents the pore pressure from reaching the static critical pore pressure in the unstimulated area. Instead, the lowered critical pore pressure by the concentrated shear stress continues to reach the pore pressure and limits the amount of the slipping area.

However, the limitations of the current numerical modeling are summarized as follows. First, two dimensional simulation overestimates the fault interaction and the enlarged fault around the injection by the simplification was the additional point of exaggerating the fault interaction. Second, the actual hypocenter of the largest magnitude earthquake was located in the deep depth. Third, the time scale is different from the field and the flow rate in 2D case can conserve farther than 3D case. However, the purpose of this study is not exact matching with the field data but suggesting the possible mechanism of LME during shut-in stage. Therefore, the suggested mechanisms can be one candidate.

Chapter 5. Conclusion

The occurrence of the largest magnitude earthquake after shut-in was shown by analyzing the semi-analytical solution and factors affecting shut-in behavior were studied. The total injected volume and properties of unstimulated area was suggested as the dominant factor to determine the occurrence of the large magnitude earthquake after shut-in. According to this effect, the shut-in phenomenon necessitates the existence of the sufficiently big anomaly where the critical pore pressure is lower than the pressure at the boundary of the stimulated area. This was because too narrow anomaly of the low critical pore pressure cannot generate the expected amount of slip.

From the numerical approach, the largest magnitude event during shut-in stage was simulated with the consideration of the shear dilation and the rupture propagation. The importance of the stress redistribution was proved and the spatial relationship of faults that can generate or prevent the large magnitude earthquake was determined.

The proposed mechanism for generating the largest magnitude earthquake during shut-in stage is basically the pressure gradient effect. However, the mechanism of conditioning the fault system into the vulnerable state for this phenomenon is important as much as the mechanism of determining the slipping area. Therefore, the stress redistribution is the important mechanism for the shut-in behavior, and the spatial relation between adjacent faults can be the effective way to determine the stress redistribution effect efficiently.

Bibliography

Abate, J., and W. Whitt (2006), A unified framework for numerically inverting Laplace transforms, *INFORMS Journal on Computing*, 18(4), 408–421.

Asanuma, H., H. Nozaki, H. Niitsuma, and D. Wyborn (2005), Interpretation of microseismic events with larger magnitude collected at Cooper Basin, Australia, *Geothermal Resources Council Transactions*, 29, 87–91.

Asanuma, H., H. Nozaki, T. Uhara, H. Niitsuma, R. Baria, and D. Wyborn (2006), Spatial and temporal distribution of larger seismic events at European and Australian HDR sites, paper presented at *Proceedings, Thirty-First Workshop on Geothermal Reservoir Engineering* Stanford University, Stanford, California, January.

Baisch, S., and H. P. Harjes (2003), A model for fluid-injection-induced seismicity at the KTB, Germany, *Geophys J Int*, 152(1), 160–170.

Baisch, S., E. Rothert, H. Stang, R. Vörös, C. Koch, and A. McMahon (2015), Continued geothermal reservoir stimulation experiments in the Cooper Basin (Australia), *Bulletin of the Seismological Society of America*, 105(1), 198–209.

Baisch, S., R. Vörös, E. Rothert, H. Stang, R. Jung, and R. Schellschmidt (2010), A numerical model for fluid injection induced seismicity at Soultz-sous-Forêts, *International Journal of Rock Mechanics and Mining Sciences*, 47(3), 405–413.

Baisch, S., R. Vörös, R. Weidler, and D. Wyborn (2009), Investigation of fault mechanisms during geothermal reservoir stimulation experiments in the Cooper Basin, Australia, *Bulletin of the Seismological Society of America*, 99(1), 148–158.

Baisch, S., R. Weidler, R. Vořořs, D. Wyborn, and L. de Graaf (2006), Induced seismicity during the stimulation of a geothermal HFR reservoir in the Cooper Basin, Australia, *Bulletin of the Seismological Society of America*, 96(6), 2242–2256.

Bissell, R., D. Vasco, M. Atbi, M. Hamdani, M. Okwelegbe, and M. Goldwater (2011), A full field simulation of the in Salah gas production and CO₂ storage project using a coupled geo-mechanical and thermal fluid flow simulator, *Energy Procedia*, 4, 3290–3297.

Bourdet, D. (2002), *Well test analysis: the use of advanced interpretation models*, Elsevier.

Charl  ty, J., N. Cuenot, L. Dorbath, C. Dorbath, H. Haessler, and M. Frogneux (2007), Large earthquakes during hydraulic stimulations at the geothermal site of Soultz-sous-For  ts, *International Journal of Rock Mechanics and Mining Sciences*, 44(8), 1091–1105.

Council, N. R. (2013), *Induced seismicity potential in energy technologies*, National Academies Press.

Davis, S. D., and C. Frohlich (1993), Did (or will) fluid injection cause earthquakes?—criteria for a rational assessment, *Seismological Research Letters*, 64(3–4), 207–224.

De Simone, S., J. Carrera, and V. Vilarrasa (2017), Superposition approach to understand triggering mechanisms of post-injection induced seismicity, *Geothermics*, 70, 85–97.

Deichmann, N., and D. Giardini (2009), Earthquakes induced by the stimulation of an enhanced geothermal system below Basel (Switzerland), *Seismological Research Letters*, 80(5), 784–798.

Deichmann, N., T. Kraft, and K. F. Evans (2014), Identification of faults activated during the stimulation of the Basel geothermal project from cluster analysis and focal mechanisms of the larger magnitude events, *Geothermics*, 52, 84–97.

Ellsworth, W. L. (2013), Injection-induced earthquakes, *Science*, 341(6142), 1225942.

Galis, M., J. P. Ampuero, P. M. Mai, and F. Cappa (2017), Induced seismicity provides insight into why earthquake ruptures stop, *Sci Adv*, 3(12).

Goebel, T. H., J. I. Walter, K. Murray, and E. E. Brodsky (2017), Comment on “How will induced seismicity in Oklahoma respond to

decreased saltwater injection rates?” by C. Langenbruch and MD Zoback, *Sci Adv*, 3(8), e1700441.

Häring, M. O., U. Schanz, F. Ladner, and B. C. Dyer (2008), Characterisation of the Basel 1 enhanced geothermal system, *Geothermics*, 37(5), 469–495.

Harris, R. A. (1998), Introduction to special section: Stress triggers, stress shadows, and implications for seismic hazard, *Journal of Geophysical Research: Solid Earth*, 103(B10), 24347–24358.

ISHIDA, M. (1974), Determination of fault parameters of small earthquake in the Kii peninsula, *Journal of Physics of the Earth*, 22(2), 177–212.

Itasca, U. (2011), Version 5.0, edited, Itasca Consulting Group, Inc., Minneapolis.

Kanamori, H., and D. L. Anderson (1975), Amplitude of the Earth's free oscillations and long-period characteristics of the earthquake source, *Journal of Geophysical Research*, 80(8), 1075–1078.

Kappelmeyer, O. (1991), European HDR project at Soultz-sous-Forêts general presentation, *Geotherm. Sci. & Tech.*, 2(4), 263–289.

Kim, K.-I., K.-B. Min, K.-Y. Kim, J. W. Choi, K.-S. Yoon, W. S. Yoon, B. Yoon, T. J. Lee, and Y. Song (2018), Protocol for induced microseismicity in the first enhanced geothermal systems project in Pohang, Korea, *Renewable and Sustainable Energy Reviews*, 91, 1182–1191, doi:<https://doi.org/10.1016/j.rser.2018.04.062>.

Kraft, T., and N. Deichmann (2014), High-precision relocation and focal mechanism of the injection-induced seismicity at the Basel EGS, *Geothermics*, 52, 59–73.

Kraft, T., P. M. Mai, S. Wiemer, N. Deichmann, J. Ripperger, P. Kästli, C. Bachmann, D. Fäh, J. Wössner, and D. Giardini (2009), Enhanced geothermal systems: Mitigating risk in urban areas, *Eos, Transactions American Geophysical Union*, 90(32), 273–274.

Lutz, B. D., A. N. Lewis, and M. W. Doyle (2013), Generation, transport, and disposal of wastewater associated with Marcellus

Shale gas development, *Water Resources Research*, 49(2), 647–656.

Majer, E., J. Nelson, A. Robertson–Tait, J. Savy, and I. Wong (2012), Protocol for addressing induced seismicity associated with enhanced geothermal systems Rep., Office of Energy Efficiency and Renewable Energy (EERE), Washington, DC (United States).

McClure, M. W. (2015), Generation of large postinjection-induced seismic events by backflow from dead-end faults and fractures, *Geophys Res Lett*, 42(16), 6647–6654.

McGarr, A. (2014), Maximum magnitude earthquakes induced by fluid injection, *Journal of Geophysical Research: Solid Earth*, 119(2), 1008–1019.

McGarr, A., and A. J. Barbour (2017), Wastewater Disposal and the Earthquake Sequences During 2016 Near Fairview, Pawnee, and Cushing, Oklahoma, *Geophys Res Lett*, 44(18), 9330–9336.

McMahon, A., and S. Baisch (2013), Case study of the seismicity associated with the stimulation of the Enhanced Geothermal System at Habanero, Australia, paper presented at Proceedings.

Mukuhira, Y., H. Asanuma, T. Ito, and M. O. Häring (2016), Physics-based seismic evaluation method: Evaluating possible seismic moment based on microseismic information due to fluid stimulation, *Geophysics*, 81(6), Ks195–Ks205.

Mukuhira, Y., H. Asanuma, H. Niitsuma, and M. O. Häring (2013), Characteristics of large-magnitude microseismic events recorded during and after stimulation of a geothermal reservoir at Basel, Switzerland, *Geothermics*, 45, 1–17.

Mukuhira, Y., C. Dinske, H. Asanuma, T. Ito, and M. O. Häring (2017), Pore pressure behavior at the shut-in phase and causality of large induced seismicity at Basel, Switzerland, *J Geophys Res–Sol Ea*, 122(1), 411–435.

Norbeck, J. H., and R. N. Horne (2018), Maximum magnitude of injection-induced earthquakes: A criterion to assess the influence of pressure migration along faults, *Tectonophysics*, 733, 108–118.

Sausse, J., C. Dezayes, L. Dorbath, A. Genter, and J. Place (2010), 3D model of fracture zones at Soultz–sous–Forets based on geological data, image logs, induced microseismicity and vertical seismic profiles, *Cr Geosci*, 342(7–8), 531–545.

Schill, E., A. Genter, N. Cuenot, and T. Kohl (2017), Hydraulic performance history at the Soultz EGS reservoirs from stimulation and long–term circulation tests, *Geothermics*, 70, 110–124.

Schoenball, M., and T. Kohl (2013), The peculiar shut–in behavior of the well GPK2 at Soultz–sous–Forêts, *GRC Trans*, 37, 217–220.

Shapiro, S. A. (2015), *Fluid–induced seismicity*, Cambridge University Press.

Tangen, G., E. G. B. Lindeberg, A. Nøttvedt, and S. Eggen (2014), Large–scale Storage of CO₂ on the Norwegian Shelf Enabling CCS Readiness in Europe, *Energy Procedia*, 51, 326–333, doi:<https://doi.org/10.1016/j.egypro.2014.07.039>.

Terakawa, T., S. A. Miller, and N. Deichmann (2012), High fluid pressure and triggered earthquakes in the enhanced geothermal system in Basel, Switzerland, *Journal of Geophysical Research: Solid Earth*, 117(B7).

Tester, J. W., B. J. Anderson, A. S. Batchelor, D. D. Blackwell, R. DiPippo, E. Drake, J. Garnish, B. Livesay, M. C. Moore, and K. Nichols (2006), *The future of geothermal energy: Impact of enhanced geothermal systems (EGS) on the United States in the 21st century*, Massachusetts Institute of Technology, 209.

Walsh, F. R., and M. D. Zoback (2015), Oklahoma’ s recent earthquakes and saltwater disposal, *Sci Adv*, 1(5), doi:[10.1126/sciadv.1500195](https://doi.org/10.1126/sciadv.1500195).

Zangerl, C., K. F. Evans, E. Eberhardt, and S. Loew (2008), Normal stiffness of fractures in granitic rock: A compilation of laboratory and in–situ experiments, *International Journal of Rock Mechanics and Mining Sciences*, 45(8), 1500–1507.

Abstract

지하로의 유체 주입은 심부 지반을 다루는 산업인 이산화탄소 지중 저장, 폐수 처리, 지열 에너지 개발, 석유 생산량 증대 기술 등에서 아주 필수적인 요소이다. 그러나 유체 주입은 유발 지진의 위험을 수반한다. 유체 주입을 중단하는 것은 유도 지진을 제어하기 위한 효과적인 방안으로 제시되어 왔으나 그 효과는 불분명했다. 스위스에 바젤에서 수행된 인공지열저류층 프로젝트의 경우, 유체 주입 중단 이후 약 5시간뒤에 발생한 지역 규모 3.4의 지진에 의해 프로젝트가 중단되었다. 이러한 문제를 해결하기 위해, 먼저 유체 주입 중단 시에 발생하는 유도지진의 물리적인 발생 기작을 밝혀내는 것이 필요하다. 본 연구에서는 불투수성 균열 암반을 가정하였으며 준해석적 방법과 2차원 개별 요소법을 이용한 수치역학적 연계 수치해석을 진행하였다. 준해석적 방법을 통해 지속적인 확산으로 인한 압력 기울기 효과(Pressure Gradient Effect)가 유체 주입 중단 후에 더 큰 규모의 지진을 발생시킬 수 있음을 보였으며, 다중 절리에 대한 수치해석을 통해 절리 간의 상호작용이 이 현상을 설명하는 하나의 방법으로 제시되었다.

주요어 : 유도 지진, 인공지열저류층, 수치자극

학 번 : 2016-23992